

Earth as a Transiting Exoplanet: A Validation of Transmission Spectroscopy & Atmospheric Retrieval Methodologies for Terrestrial Exoplanets

JACOB LUSTIG-YAEGER,^{1,2} VICTORIA S. MEADOWS,^{3,2} DAVID CRISP,^{4,2} MICHAEL R. LINE,^{5,2} AND TYLER D. ROBINSON^{6,7,2}

¹*Johns Hopkins University Applied Physics Laboratory, Laurel, MD 20723, USA*

²*NASA NExSS Virtual Planetary Laboratory, Box 351580, University of Washington, Seattle, Washington 98195, USA*

³*Department of Astronomy and Astrobiology Program, University of Washington, Box 351580, Seattle, Washington 98195, USA*

⁴*Jet Propulsion Laboratory, California Institute of Technology, Earth and Space Sciences Division, Pasadena, CA 91011, USA*

⁵*School of Earth and Space Exploration, Arizona State University, P.O. Box 871404, Tempe, AZ 85287-1404, USA*

⁶*Lunar & Planetary Laboratory, University of Arizona, Tucson, AZ 85721, USA*

⁷*Department of Astronomy and Planetary Science, Northern Arizona University, Flagstaff, AZ 86011, USA*

(Accepted August 22, 2023)

Submitted to PSJ

ABSTRACT

The James Webb Space Telescope (JWST) will enable the search for and characterization of terrestrial exoplanet atmospheres in the habitable zone via transmission spectroscopy. However, relatively little work has been done to use solar system data, where ground truth is known, to validate spectroscopic retrieval codes intended for exoplanet studies, particularly in the limit of high resolution and high signal-to-noise (S/N). In this work, we perform such a validation by analyzing a high S/N empirical transmission spectrum of Earth using a new terrestrial exoplanet atmospheric retrieval model with heritage in Solar System remote sensing and gaseous exoplanet retrievals. We fit the Earth's 2 – 14 μm transmission spectrum in low resolution ($R = 250$ at 5 μm) and high resolution ($R = 100,000$ at 5 μm) under a variety of assumptions about the 1D vertical atmospheric structure. In the limit of noiseless transmission spectra, we find excellent agreement between model and data (deviations $< 10\%$) that enable the robust detection of H₂O, CO₂, O₃, CH₄, N₂, N₂O, NO₂, HNO₃, CFC-11, and CFC-12 thereby providing compelling support for the detection of habitability, biosignature, and technosignature gases in the atmosphere of the planet using an exoplanet-analog transmission spectrum. Our retrievals at high spectral resolution show a marked sensitivity to the thermal structure of the atmosphere, trace gas abundances, density-dependent effects, such as collision-induced absorption and refraction, and even hint at 3D spatial effects. However, we used synthetic observations of TRAPPIST-1e to verify that the use of simple 1D vertically homogeneous atmospheric models will likely suffice for JWST observations of terrestrial exoplanets transiting M dwarfs.

Keywords: planets and satellites: atmospheres – planets and satellites: individual (Earth) – planets and satellites: terrestrial planets – techniques: spectroscopic

1. INTRODUCTION

Solar System planets provide a powerful opportunity to validate both the astronomical observing strategies and the theoretical modeling approaches required to characterize distant exoplanets. Such ground-truth ef-

forts are becoming increasingly important in the era of the James Webb Space Telescope (JWST), which can collect relatively high signal-to-noise (S/N) spectra of gaseous exoplanets (e.g. [Greene et al. 2016](#); [The JWST Transiting Exoplanet Community Early Release Science Team et al. 2022](#)) and sufficient S/N spectra of rocky exoplanets to enable atmospheric detection and modest atmospheric characterization for the first time (e.g. [Morley et al. 2017](#); [Wunderlich et al. 2019](#); [Lustig-Yaeger et al. 2019](#); [Faucher et al. 2019](#); [Pidhorodetska et al.](#)

2020; Suissa et al. 2020; Gialluca et al. 2021). While these next-generation observations promise higher precision on exoplanetary atmospheres, they may present a greater challenge to interpret correctly in the presence of complicated physical, chemical, and three dimensional effects. In this paper, we analyze the observed transmission spectrum of Earth, recently published by Macdonald & Cowan (2019), using a state-of-the-art terrestrial exoplanet atmospheric retrieval code with extensive Solar System heritage. We examine common modeling assumptions used throughout the field, and then relate the observations to upcoming opportunities to study transiting Earth-like exoplanets on the path to constraining habitability and the presence of life beyond Earth.

Shifting our perspective to envision Solar System planets as exoplanets has already helped to fundamentally shape the outlook for future exoplanet observations. At the dawn of the exoplanet era, Sagan et al. (1993) analyzed a combination of spectroscopic and imaging observations of Earth from the *Galileo* spacecraft to argue for the remote detection of life on Earth based on detection of atmospheric oxygen and methane, ocean glint, and the vegetation red edge. More recently time-dependent reflected-light observations of Earth using the Extrasolar Planet Observation and Deep Impact Extended Investigation (EPOXI) mission (Livengood et al. 2011) were used to demonstrate a method of spatially mapping terrestrial exoplanets using rotation-induced photometric variability (e.g. Cowan et al. 2009; Fujii et al. 2011; Cowan & Strait 2013; Fujii et al. 2017). Observations of Earth using the Deep Space Climate Observatory (DSCOVR) have helped to mature these spatial mapping methods (Jiang et al. 2018; Fan et al. 2019; Aizawa et al. 2020; Kawahara 2020; Kawahara & Masuda 2020; Gu et al. 2021, 2022). The EPOXI observations have also been used to validate high-fidelity, 3D models of Earth (Robinson et al. 2010, 2011) that have been used to predict the strength of the ocean glint signal for Earth-analog exoplanet observations (Robinson et al. 2010; Lustig-Yaeger et al. 2018). These predictions were further validated using Lunar CRater Observation and Sensing Satellite (LCROSS) observations of Earth, which successfully detected ocean glint (Robinson et al. 2014a), opening a path for robust habitability assessments in the future. Measurements of Solar System bodies as a function of illumination, including Jupiter (Mayorga et al. 2016), Saturn (Dyudina et al. 2005, 2016), and the Galilean satellites (Mayorga et al. 2020), have brought to light the importance of phase-resolved observations for comparative planetology with future direct-imaging telescopes.

Of more direct relevance to JWST observations, Earth and Solar System planetary observations have been reanalyzed to produce exoplanet-analog transmission spectra that can be used to test our understanding and models of exoplanet transit phenomena. Measurements of Earthshine reflected off the moon during lunar eclipses have been used to study the characteristic spectroscopic observables of Earth as seen in a transit viewing geometry (Pallé et al. 2009; Vidal-Madjar et al. 2010; Ugolnikov et al. 2013; Arnold et al. 2014; Yan et al. 2015; Kawauchi et al. 2018; Youngblood et al. 2020). In addition, solar occultation limb-sounding measurements have been used to construct exoplanet-analog transmission spectra for Saturn (Dalba et al. 2015), Titan (Robinson et al. 2014b; Tribbett et al. 2021), and Earth (Schreier et al. 2018; Macdonald & Cowan 2019). These Solar System transmission spectra are particularly salient at present because transiting exoplanets will likely be the first terrestrial targets in the next few years to afford spectroscopic atmospheric characterization (National Academies of Sciences, Engineering, and Medicine 2018).

Current and upcoming transmission spectroscopy observations of the TRAPPIST-1 system (Gillon et al. 2016, 2017; Luger et al. 2017) with JWST are predicted to probe the composition of terrestrial exoplanet atmospheres for the first time (Barstow & Irwin 2016; Morley et al. 2017; Batalha et al. 2018; Krissansen-Totton et al. 2018; Wunderlich et al. 2019; Lustig-Yaeger et al. 2019; Wunderlich et al. 2020; May et al. 2021; Lin et al. 2021; Fauchez et al. 2022; Mikal-Evans 2022; Krissansen-Totton & Fortney 2022; Rotman et al. 2023). These observations will be analyzed with atmospheric retrieval models that are designed to infer the physical and chemical state of the planetary atmosphere, including presence and abundance of gases, from spectroscopic measurements. For these rocky exoplanet observations, attempts will be made to look for signs of past evolutionary processes (e.g., Lincowski et al. 2018, 2019; Lustig-Yaeger et al. 2019; Loftus et al. 2019) and assess the surface habitability and presence of biosignatures (e.g., Krissansen-Totton et al. 2018; Wunderlich et al. 2019, 2020; Meadows et al. 2023).

Over the past decade and a half, numerous atmospheric retrieval models have been developed to interpret the transmission and thermal emission spectra of gas giant exoplanets (Irwin et al. 2008; Madhusudhan & Seager 2009; Line et al. 2013; Benneke & Seager 2013; Waldmann et al. 2015; Cubillos et al. 2016; Lavie et al. 2016; MacDonald & Madhusudhan 2017; Howe et al. 2017; Kitzmann et al. 2019; Zhang et al. 2019; Damiano & Hu 2020) and to validate different retrieval mod-

els against one another (Kreidberg et al. 2015; Barstow et al. 2020) (see MacDonald & Batalha (2023) for a more complete catalog of retrieval codes). Additionally, critical retrieval work has been done in preparation for data capable of characterizing rocky exoplanet atmospheres using, for example, JWST observations (Barstow et al. 2016; Barstow & Irwin 2016; Krissansen-Totton et al. 2018; Lin et al. 2021; Mikal-Evans 2022) and next generation observing capabilities (Feng et al. 2018; Quanz et al. 2019; Tremblay et al. 2020). However, relatively few studies (e.g., Robinson & Salvador 2023) have been performed to validate terrestrial retrieval models and their common underlying assumptions using exoplanet analog observations within the solar system, particularly over a broad wavelength range and using high precision observations. Thus, to fully realize the scientific value of upcoming terrestrial exoplanet observations it is critical to validate these retrieval codes on observations with known ground-truth, before (or in parallel with) attempts to understand the unexpected alien environments of exoplanets.

The empirical transit transmission spectrum of Earth from MacDonald & Cowan (2019) (hereafter M&C19) provides a JWST-relevant wavelength range with the highest signal-to-noise ratio (S/N) and spectral-resolution to date, with which to gauge the efficacy of transmission spectroscopy observations and atmospheric retrieval inference methods for characterizing Earth-like exoplanet atmospheres for habitability and biosignatures. M&C19 post-processed Earth solar occultation measurements observed with the Canadian low-Earth orbit satellite, SCISAT, using the *Atmospheric Chemistry Experiment Fourier Transform Spectrometer* (ACE-FTS; Bernath et al. 2005; Hughes et al. 2014). The resulting 2 – 14 μm transmission spectrum of Earth, shown in the upper panel of Figure 1, contains numerous absorption features from characteristic molecules in Earth’s atmosphere, such as CO_2 , H_2O , CH_4 , and O_3 , among many others (see Schreier et al. 2018). The broad wavelength range overlaps significantly with that of JWST’s primary exoplanet transmission spectroscopy instruments, including, NIRSpec, NIRISS, and MIRI, making it a particularly useful analog for upcoming observations. The high S/N of the Earth spectrum provides an opportunity to test best-case-scenarios for transmission spectroscopy with data that does not suffer from astrophysical (e.g. temporal, spatial, and spectral stellar variability) or astronomical (e.g. detector white and red noise) limitations of true exoplanet observations. The high spectral resolution affords the ability to bin the spectrum down to a variety of lower resolutions that are applicable to upcoming

exoplanet observations, as well as to validate transmission spectroscopy retrievals at a high-resolution that is analogous to current and upcoming ground-based exoplanet observations (e.g., Snellen et al. 2013; Brogi et al. 2014; Snellen et al. 2017; Brogi & Line 2019; Webb et al. 2020).

In this paper, we describe a new terrestrial (exo)planet atmospheric retrieval model, SMARTER, based on a physically-rigorous, line-by-line radiative transfer code that has been previously validated on emission and reflected spectra from Solar System terrestrials. This model has the capability to analyze UV to millimeter wave transmission, reflected light and emission data for exoplanets with a wide range of atmospheric compositions, temperatures and pressures. Here we validate the code using Earth’s empirical transmission spectrum from M&C19. In addition to validating our model and common modeling assumptions, we explore the achievable constraints on Earth’s atmospheric composition and temperature structure at low and high spectral resolution, and using different levels of observational noise to link our findings to current and upcoming observations with JWST.

In the next section, we describe our methods, including information about the transmission spectrum from M&C19 (Section 2.1) and descriptions of our atmospheric retrieval model (Section 2.2). In Section 3, we describe our results. We discuss our findings in Section 4 and present our conclusions in Section 5.

2. METHODS

2.1. Observed Data

Macdonald & Cowan (2019) processed solar occultation measurements of the Earth’s atmosphere to produce an altitude-integrated and limb-averaged transmission spectrum from an observer perspective that is analogous to transiting exoplanets (Seager & Sasselov 2000; Charbonneau et al. 2002). The original measurements were made by the Canadian low-Earth orbit satellite, SCISAT, using the *Atmospheric Chemistry Experiment Fourier Transform Spectrometer* (ACE-FTS; Bernath et al. 2005; Hughes et al. 2014; Boone & Bernath 2019). ACE-FTS is a high resolution spectrograph that observes between approximately 700–4400 wavenumbers (2.27–14.3 μm) with a full-width-at-half-maximum (FWHM) of 0.02 cm^{-1} and a sampling resolution of 0.0025 cm^{-1} . This corresponds to a spectral resolving power of $R = 100,000$ at 5 μm (2000 cm^{-1}). Spectra were recorded of Sunlight passing through the Earth’s atmosphere as a function of time during sunrises and sunsets. The transmittance, \mathcal{T} , of Earth’s atmosphere can be derived as a function of both wavelength

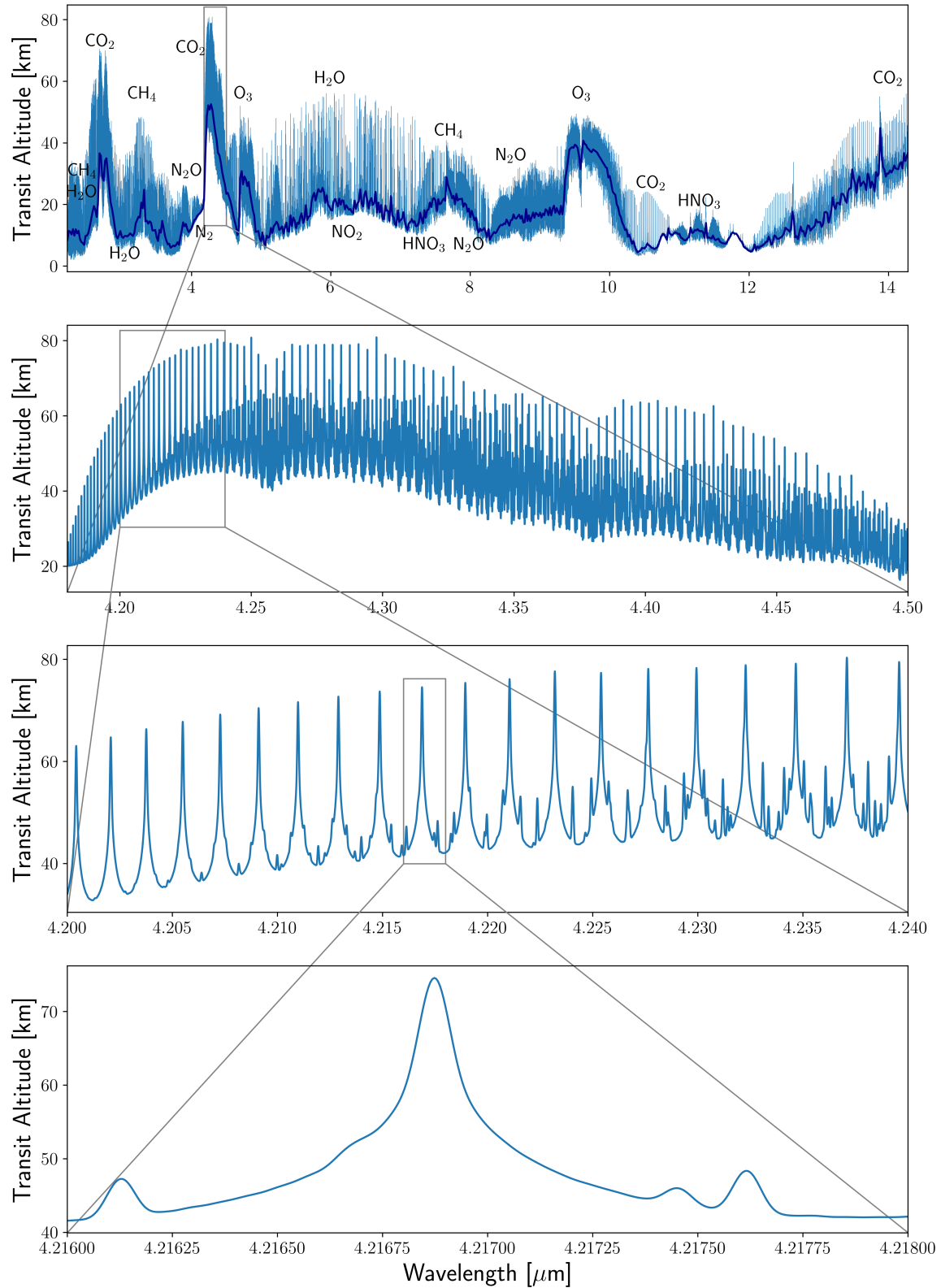


Figure 1. Empirical transmission spectrum of the cloudless Earth from [Macdonald & Cowan \(2019\)](#). The top panel shows the full wavelength range in high-resolution (light blue) and binned to a lower resolution ($\Delta\lambda = 0.02 \mu\text{m}$; dark blue). The lower panels zoom into the $4.2 \mu\text{m}$ CO_2 band, showing progressively smaller wavelength ranges and highlighting the fully resolved spectral lines with no apparent observational noise. The data behind this figure is available at [DOI: 10.5281/zenodo.8280710](https://doi.org/10.5281/zenodo.8280710) ([Macdonald & Cowan 2023](#)) which was obtained from the ACE-FTS Atmospheric Atlases ([Hughes et al. 2014](#)) at <http://www.ace.uwaterloo.ca/atlas.php>.

and altitude by dividing out the unattenuated spectrum of the Sun acquired from observations taken just prior to atmospheric occultation. These data products support the main objective of the mission to study the vertical distribution of trace gases in the Earth’s atmosphere.

M&C19 calculated the transmission spectrum of the Earth as if it were an exoplanet by integrating the ACE-FTS transmittance data from the bottom to the top of the atmosphere using the approach described in Robinson et al. (2014b) for Titan and Dalba et al. (2015) for Saturn. M&C19 selected for only cloud-free sightlines through the Earth’s atmosphere and averaged approximately 800 datasets spanning five latitudinal regions—Arctic summer and winter ($60 - 85^\circ$ N), mid-latitude summer and winter ($30 - 60^\circ$ N), and the tropics (30° S – 30° N)—to mimic the limb-integrated stellar light transmitted through exoplanet atmospheres during primary transit. The final published transmission spectrum has S/N ≈ 8000 in the continuum. Although M&C19 explored modifications to their resulting transmission spectrum due to refraction, their data, as well as the spectrum analyzed in this paper, does not possess the critical refraction boundary that limits the spectrum from probing below ~ 15 km for an Earth-Sun exoplanet analog (Misra et al. 2014; B  tr  mieux & Kaltenecker 2014). As a result, we are able to probe deeper into the Earth’s atmosphere than a true Earth-Sun-analog exoplanet observation, where the observer can be assumed to be infinitely far away. While the empirical spectrum from M&C19 and analyzed in this work does not contain cloudy sightlines, we refer readers to the recent work of Doshi et al. (2022) for a detailed analysis of the cloudy Earth spectrum derived from the same SCISAT measurements.

Figure 1 shows the empirical transmission spectrum of Earth from Macdonald & Cowan (2019)¹. The broad wavelength coverage spanning $2 - 14 \mu\text{m}$ contains spectral features from over a dozen different molecules (Bernath et al. 2005; Bernath 2017; Schreier et al. 2018). The top panel shows the spectrum at the native high resolution (light blue) and binned to a lower resolution of $\Delta\lambda = 0.02 \mu\text{m}$ (dark blue; $R = 250$ at $5 \mu\text{m}$). The zoomed subpanels focus on the $4.3 \mu\text{m}$ CO_2 band and showcase the extremely high resolution and high S/N of the spectrum. Most spectral lines appear to be fully resolved. The bottom-most panel shows that there is no visible scatter in the data, reinforcing its high S/N (~ 8000) and lack of white noise. With its high resolution and S/N, this spectrum should be ideal for validat-

ing a spectral retrieval code designed for transmission spectroscopy.

2.2. Retrieval Model

In this work, we use a novel atmospheric retrieval code developed specifically to interpret the spectra of terrestrial exoplanets. Our retrieval model differs from other state-of-the-art retrieval codes primarily in the treatment of radiative transfer, for which we use the robust line-by-line Spectral Mapping Atmospheric Radiative Transfer (SMART) model (Meadows & Crisp 1996; Crisp 1997). Due to the rigor of the radiative transfer, the SMART Exoplanet Retrieval (SMARTER) code has been developed to use a variety of different Bayesian retrieval approaches to solve the inverse problem so that the complexity of the physical and statistical methods can be appropriately balanced to achieve a computationally tractable problem. In this section, we first describe the SMARTER forward model used for exoplanet transit transmission spectroscopy (§ 2.2.1), and then describe the SMARTER inverse modeling suite (§ 2.2.2).

2.2.1. Forward Model

The SMARTER forward model was designed with a modular approach capable of leveraging the many radiative transfer capabilities of SMART to perform exoplanet retrievals. As a result, SMARTER can run atmospheric retrievals for both terrestrials and Jovians using transmission, thermal emission, and reflected-light spectra. However, in this work, we focus exclusively on transmission spectroscopy of the Earth and Earth-like exoplanets.

Radiative Transfer—SMARTER uses the Spectral Mapping Atmospheric Radiative Transfer (SMART) model as its forward model (developed by D. Crisp; Meadows & Crisp 1996; Crisp 1997). SMART was originally designed to accelerate radiative transfer calculations in planetary atmospheres where both gas absorption and multiple scattering by gases, clouds and aerosols contribute to extinction. In spectral regions dominated by vibration-rotation transitions of gases (i.e., spectral lines), a very fine spectral grid is needed to resolve the spectral structure of the atmospheric optical properties. If multiple scattering is also an important source of extinction in these spectral regions, a computationally-expensive multiple scattering calculation must be performed at each monochromatic spectral grid point (a single, fine wavelength point) to accurately evaluate the radiances and fluxes within the atmosphere (Meadows & Crisp 1996; Crisp 1997; Arney et al. 2016).

To accelerate these calculations, SMART exploits the fact that many spectral grid points within wide spec-

¹ The published spectrum is available at DOI: 10.5281/zenodo.8280710 (Macdonald & Cowan 2023).

tral regions have very similar optical properties at all points along the optical path. After generating the optical properties on high-resolution spectral grid, SMART identifies those spectral grid points with nearly identical optical properties along the entire atmospheric optical path (West et al. 1990; Meadows & Crisp 1996). Spectral grid points with optical properties within a specified range of values are mapped into a series of quasi-monochromatic spectral bins. For example, the binning criteria might specify that only grid points with layer-integrated optical depths, single scattering albedos and scattering phase functions with 25% of the mean values of a bin are included in that bin. Once the optical properties are binned, radiances and their Jacobians (i.e., the first derivative of the radiances with respect to changes in the atmospheric temperatures or optical properties) are derived for the mean values of the optical properties in each bin. The Jacobians provide a linear correction to radiances for each bin when these values are mapped back to original monochromatic spectral grid points. This spectral binning and remapping approach produces high-resolution radiance spectra and typically reduces the number of radiative transfer calculations by a factor of 10 to 1000, depending on the user-specified spectral binning criteria. There are four unique binning tolerance parameters defined in terms of the fractional error in optical depth, co-single scattering albedo, aerosol asymmetry factor, and surface optical properties (e.g., surface albedo). However, only the optical depth binning parameter is relevant to this work (and only for simulations in Appendix A).

SMART was originally developed for plane-parallel radiative transfer calculations in planetary atmospheres (e.g., Meadows & Crisp 1996; Robinson et al. 2011; Arney et al. 2016; Meadows et al. 2018b; Lincowski et al. 2021). For those applications, the DIScrete Ordinate Radiative Transfer code (DISORT; Stammes et al. 1988, 2017) was used to perform the radiative transfer calculations for each bin. More recently, SMART was extended to perform transit calculations (Misra et al. 2014; Robinson 2017a). That is the version that is used here and it is independent of DISORT. The transmission spectrum calculations can be performed using one of three methods (Robinson 2017a): (1) geometric optics using straight rays, (2) ray tracing (with the option for the refraction of stellar rays passing through the atmosphere), and (3) Monte Carlo numerical integration to account for forward-scattering by aerosol particles. For the ray-tracing option without refraction, used in most of the simulations presented here, the full-resolution monochromatic optical properties generated by SMART are used, without the binning and remapping operations

described above. When ray tracing is used with refraction (See Appendix A), the full-resolution monochromatic optical properties are used, but the optical path length calculations assume that the refraction is constant within each bin. The Monte Carlo method uses the full spectral binning and remapping operations to improve efficiency. Here we use the ray tracing methods for all cases.

Typically, refraction would be used for transit calculations, but in this case we turn refraction off unless otherwise noted because the solar occultation geometry of Earth’s transmission spectrum from M&C19 permits access to the near-surface atmosphere that would be restricted by the critical refraction boundary for a true Earth-analog exoplanet (Bétrémieux & Kaltenegger 2014; Misra et al. 2014). We explore the impacts of refraction on the optical path length using high-resolution spectral models with and without refraction in Appendix A, as discussed later in Section 3.2, but we found that it had little impact on the results.

Gas absorption cross sections are used with SMART to account for (1) vibrational–rotational transitions in the optical and infrared, (2) continuum absorption in the UV, and (3) collision-induced absorption (CIA) bands. SMART depends on the Line-By-Line ABSorption Coefficient (LBLABC) code to calculate molecular vibrational-rotational transition absorption coefficient input files for the radiative transfer (developed by D. Crisp; Meadows & Crisp 1996). LBLABC takes information about the input atmospheric state—the temperature versus pressure (TP) profile, vertical gas mixing ratio, mean molecular weight of the atmosphere, and radius and surface gravity of the planet—and combines it with HITRAN line-parameter and isotope information to calculate the gas absorption coefficients as a function of pressure, temperature, and wavenumber. Unless otherwise stated, we use the HITRAN2016 line list (Gordon et al. 2017) as an input for LBLABC and our subsequent radiative transfer calculations with SMART. LBLABC uses nested spectral grids to fully resolve the narrow cores of each absorption line and to resolve the far wings of the lines at every atmospheric layer over a very large range of line-center distances. Line contributions are calculated up to 1000 cm^{-1} from the line center for H_2O and CO_2 to capture the full wings of strong lines; all other gases have a 50 cm^{-1} wing cutoff to speed up calculations where contribution from the far wings is negligible. LBLABC employs different line profiles as a function of distance from the line core. LBLABC uses a Voigt line shape (Humlíček 1982) within 40 Doppler half-widths of the line center, and a van Vleck-Weisskopf profile (Van Vleck & Weisskopf 1945) beyond that for all gases except H_2O , CO_2 ,

and O_2 . Empirically determined χ correction factors are used in the far wings for H_2O (Clough et al. 1989) and CO_2 (Fukabori et al. 1986; Perrin & Hartmann 1989; Pollack et al. 1993) to reproduce the effects of quantum-mechanical line mixing, a collisional effect that occurs for overlapping lines of a given molecular species (Rao 2012). For O_2 , the super-Lorentzian line shape from Hirono & Nakazawa (1982) is used with an exponent of 1.958. LBLABC features the ability to simulate line absorption coefficients for fixed temperature offsets from the given TP profile, which SMART can interpolate between for added flexibility when deviating from an initial temperature structure. This can be used to generate a single set of line absorption coefficients that may be interpolated to yield estimates that are used over a broad range of atmospheric temperature structures that may be explored by the retrieval, without requiring LBLABC to be run multiple times.

The internal wavenumber resolution of SMART is designed to completely resolve the spectral structure of the atmospheric and surface optical properties. In spectral regions where the atmospheric and surface optical properties vary slowly with wavelength, such as the near UV, the resolving power can be as low as 100. At infrared wavelengths populated by the gas vibration-rotation transitions, the spectral resolution is set by gas absorption cross-section algorithm, LBLABC. For each spectral line, LBLABC finds the atmospheric level where the Voigt line full-width-at-half-maximum (FWHM) is the smallest. It then resolves the FWHM of this “line core” region with at least 8 spectral grid points. At larger distances from the line center, the distance between spectral grid points increases in a geometric series, such that the grid spacing increases 25% for each point, such that the line wings are well resolved, with a few hundred (<512) points. LBLABC then maps this individual-line spectral grid onto a common spectral grid that is used for all spectral lines at all levels of the atmosphere. This grid can have a spectral resolving power as high as 10^7 .

One important exception to the above is implemented for instances where the spectral resolution of the data is significantly lower than typical line widths. In this case, the line absorption coefficient files from LBLABC may be resampled to a lower resolution, which then sets the resolution of SMART and can significantly speed up retrieval calculations with SMARTER. For our retrievals on spectra with simulated noise that use the nested sampling retrieval approach (Section 3.1.3 and Section 3.3), we resample our molecular line absorption coefficients to a resolution of 0.1 cm^{-1} .

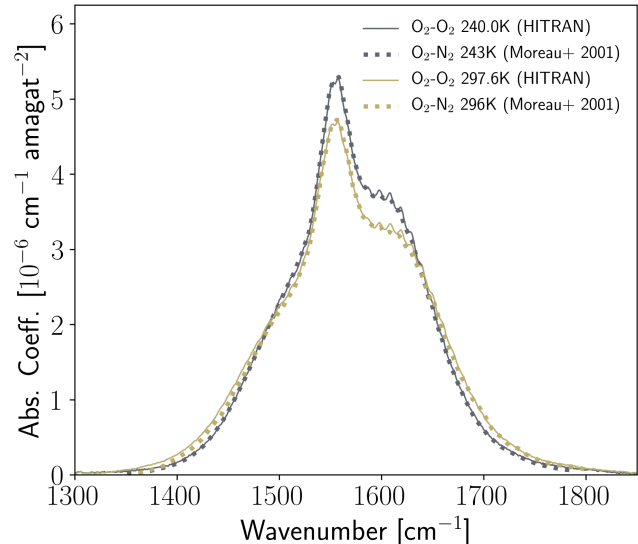


Figure 2. A comparison between the $6\mu\text{m}$ O_2-N_2 CIA band from Moreau et al. (2001) and the $6\mu\text{m}$ O_2-O_2 CIA band from HITRAN 2016 (Gordon et al. 2017). At Earth-like temperatures and pressures, the O_2-N_2 and O_2-O_2 CIA bands appear to agree in intensity suggesting that the O_2-O_2 absorption coefficient can be accurately used for O_2-N_2 .

We incorporate UV and visible cross sections from the MPI-Mainz UV/VIS Spectral Atlas of Gaseous Molecules (Keller-Rudek et al. 2013) as described in Lincowski et al. (2018). We use HITRAN infrared absorption cross-sections (Kochanov et al. 2019) for two chlorofluorocarbons (CFCs): CCl_3F (CFC-11; Harrison 2018) and CCl_2F_2 (CFC-12; Harrison 2015). CIA data are used for CO_2-CO_2 (Moore 1972; Kasting et al. 1984; Gruszka & Borysow 1997; Baranov et al. 2004; Wordsworth et al. 2010; Lee et al. 2016), O_2-O_2 (Greenblatt et al. 1990; Hermans et al. 1999; Maté et al. 1999; Gordon et al. 2017), and N_2-N_2 (Lafferty et al. 1996; Schwieterman et al. 2015b). Following Fauchez et al. (2020), we include O_2-N_2 CIA at $6\mu\text{m}$ by assuming that it is equivalent in strength to the corresponding O_2-O_2 CIA band at $6\mu\text{m}$, which is incorporated from HITRAN (Karman et al. 2019). In Figure 2 we compare the laboratory derived CIA absorption coefficients for O_2-N_2 at $6\mu\text{m}$ from Moreau et al. (2001) with that of O_2-O_2 from HITRAN (Karman et al. 2019). At Earth temperatures and pressures, using O_2-O_2 as a proxy for O_2-N_2 appears to be valid.

SMART and LBLABC were developed for Solar System terrestrial planet atmospheres and have been rigorously validated on the Earth (Robinson et al. 2011) and Venus (Meadows & Crisp 1996; Crisp et al. 1996; Arney et al. 2014; Robinson & Crisp 2018) reflected and thermal observations. SMART has been used to simulate the spectra

of a rich diversity of exoplanet environments, including the spectra of M dwarf habitable planets (Segura et al. 2003, 2005; Meadows et al. 2018b) and uninhabitable planets (Lincowski et al. 2018, 2019), habitable hazeshrouded exoplanets (Arney et al. 2016, 2017), and high-altitude clouds in the H₂-dominated mini-Neptune exoplanet, GJ1214b (Charnay et al. 2015). SMART also functions as the radiative transfer core for the VPL Climate Model (Robinson & Crisp 2018; Lincowski et al. 2018).

Baseline Transmission Forward Models—We employ two different transit transmission spectroscopy forward models in this work. Both forward models call SMART for the radiative transfer and make a number of simplifying assumptions to limit the volume of parameter space that the retrieval must traverse. However, each model differs in the treatment of vertical atmospheric profiles in order to test different modeling approaches and their underlying assumptions.

The first forward model uses 1D vertical atmospheric temperature and gas mixing ratio profiles provided by the user and the retrieval fits for scaling factors that shift the entire profile to larger or smaller values without changing the shape, similar to the approach used by Barstow et al. (2016). We refer to this as the “scaled profiles” model and “Model 1”. This model makes a strong *a priori* assumption about the shape of the 1D vertical profiles, but it offers a solid foundation to test the accuracy of our retrieval model on high quality data, to examine how well a 1D atmosphere can reproduce observations of a 3D planet, and to compare against our model with a homogeneous vertical structure. We note that for instances using Model 1, where the scale factor is sufficiently large so as to make any mixing ratio exceed unity, that value is capped at one. However, if the sum of all gas mixing ratios exceeds one, then the sample is rejected by the forward model.

The second forward model assumes that the 1D atmosphere is isothermal with evenly mixed gas abundance profiles—a common set of assumptions in the exoplanet atmospheric retrieval community. We refer to this as the “evenly-mixed” model and “Model 2”. Although such isothermal atmospheres are unphysical, and indeed mixing ratio biases have been reported in retrieval tests of hot Jupiter atmospheres (Rocchetto et al. 2016), transmission spectroscopy is only weakly sensitive to the atmospheric thermal structure (Kempton et al. 2017), and it remains unclear if JWST will have the precision to justify more complex TP profile retrievals for rocky exoplanets. This model offers the opportunity to test these common exoplanet assumptions and examine how a real

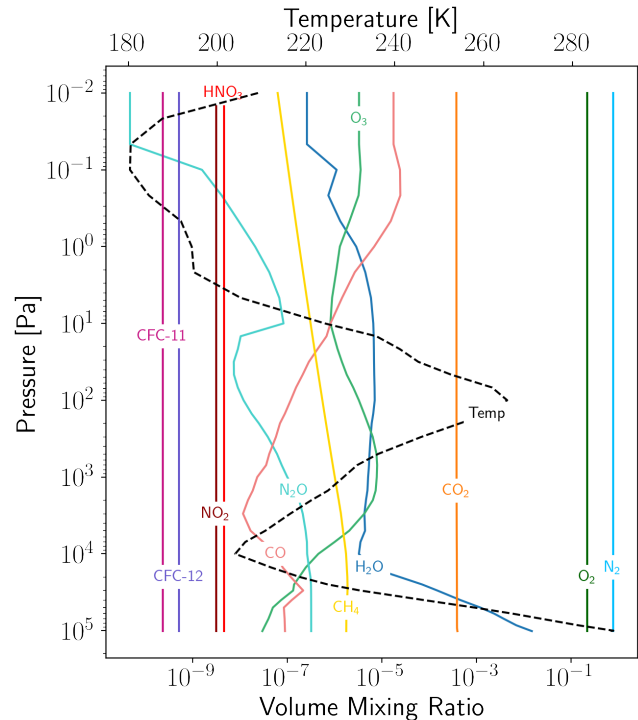


Figure 3. Earth’s approximate 1D atmospheric thermal structure and composition. The temperature structure (dashed black) is shown along the top x-axis and the gas mixing ratios are shown along the bottom x-axis, both as a function of pressure. This model is used to inform the initialization of our retrievals.

exoplanet-analog observation is interpreted through the lens of this simplified model.

We use a globally-averaged 1D atmospheric structure for Earth as a starting point for our retrievals and a basis for comparison to the known Earth atmospheric structure and composition. Figure 3 shows Earth’s average 1D atmospheric vertical thermal structure and composition acquired from satellite data for the VPL Earth Model (Robinson et al. 2011) to reproduce the EPOXI flyby of Earth in March and April of 2008. We use these profiles as the starting point for our retrievals. Model 1 linearly scales each of these profiles to improve the fit. Model 2 is initialized with evenly mixed atmospheric profiles that are calculated as log-pressure-weighted averages using a weighting kernel that is given by,

$$w = \frac{1}{\log_{10}(P [\text{bar}]) - \log_{10}(0.1 [\text{bar}])^2 + \epsilon}, \quad (1)$$

which favors pressures near 0.1 bar (10⁴ Pa), approximately where transmission spectra are most sensitive, with $\epsilon = 0.1$ dex (10^{0.1} \approx 1.26) to control the width of averaging kernel around 0.1 bar. In addition to the gases included in the VPL Earth Model (H₂O, CO₂, O₃, O₂, N₂, CH₄, CO, and N₂O), we also include HNO₃,

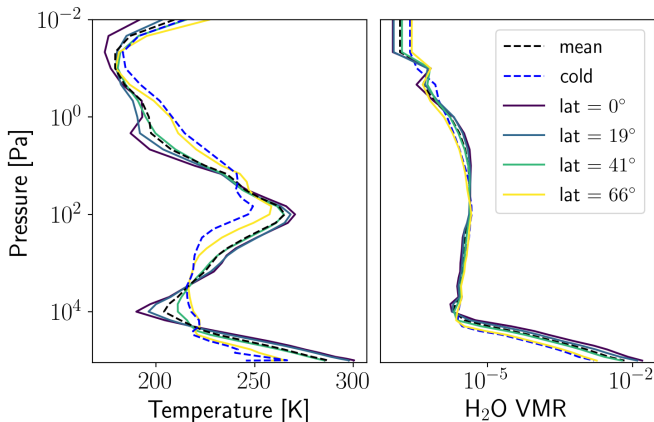


Figure 4. Characteristic thermal (left) and water (right) profiles of Earth’s atmosphere. The profiles are derived from satellite data and were acquired to match the dates of the EPOXI Earth flyby in 2008 (see [Robinson et al. 2011](#)). Each latitude plotted represents the globally averaged vertical profile for all HEALPix bins with the corresponding north and south latitudes.

NO_2 , CCl_3F (CFC-11), and CCl_2F_2 (CFC-12) because they corrected notable residuals in our initial tests. For HNO_3 and NO_2 , we use evenly mixed atmospheric profiles as shown in Fig. 3, initialized using best estimates from the literature. For HNO_3 , we initialize at 10 ppb VMR based on a measurement from [Hanke et al. \(2003\)](#), for NO_2 , we use 5 ppb VMR, which is consistent with measurements in urban areas ([Lamsal et al. 2013](#); [Kopparapu et al. 2021](#)), and for CFC-11 and CFC-12 we used 230 ppt and 510 ppt, respectively, consistent with findings from [Kellmann et al. \(2012\)](#).

Unless otherwise stated, we fix the TP profile in our forward model to the mean Earth 1D TP profile shown in Figure 3. An important caveat to this is when we fit for an isothermal TP profile. Additionally, to provide an initial exploration of vertical sensitivity without performing expensive vertically-resolved retrievals, for a subset of our retrieval experiments, we run multiple cases with different globally- and latitudinally-averaged temperature and water profiles. Figure 4 shows four characteristic TP profiles and water profiles that represent a substantial portion of the spatial variance within the data acquired for use with the VPL Earth Model ([Robinson et al. 2011](#)). These characteristic profiles correspond to averages within broad equatorially symmetric latitudinal bands (e.g. our 19° profile corresponds to an average of both 19° N and 19° S latitudinal bins). Also shown are the average Earth profiles (black dashed line) from Figure 3 and a particular profile with the coldest surface in the VPL Earth Model database (blue dashed line). There is substantial variability between the different TP profiles at all relevant pressures from

the surface to the upper atmosphere. The water profiles agree well above the tropopause and show the greatest difference in the troposphere, where more water vapor is seen closer to the equator.

We used a nominal SMART simulation setup for our high and low resolution Earth retrievals that, unless otherwise stated, remained fixed throughout these experiments. We fixed the mean molecular weight of the atmosphere at 29 g/mol, consistent with the Earth atmosphere, we fixed the surface pressure at 1 bar, and the solid-body planet radius and mass are fixed at $1 R_\oplus$ and $1 M_\oplus$, respectively. This implicitly fixed the surface gravity at 9.81 m/s^2 . We also placed the Earth at 1 AU from the Sun, which has a stellar radius of $1 R_\odot$. These simplifying assumptions allow us to specifically focus on the retrieval of spectroscopic features while neglecting numerous parameters that are important for exoplanet atmospheric retrievals—such as the mean molecular weight and surface gravity, which are degenerate for transmission spectroscopy with the atmospheric temperature via the scale height ([Barstow & Heng 2020](#)). These important considerations are beyond the scope of this study. We set the transit impact parameter to zero, and we turned off the stellar and thermal source functions to only simulate the transmission spectrum. Finally, for our ray tracing refraction simulations, we used an optical depth binning parameter for SMART of 0.75, which is large, but our tests have shown that negligible errors ($< 1\%$) are introduced for transmission calculations even with large spectral mapping bin tolerances. For the majority of our experiments we opted to have our retrieval forward model return the transmission spectrum in units of altitude in kilometers above the surface (i.e., the effective transit altitude) to enhance physical intuition with respect to the planetary environment, rather than convert the data into units of transit depth, $(R_p/R_s)^2$. However, JWST relevant retrievals in Section 3.3 were performed in the standard exoplanet transit depth.

The final step in the SMARTER forward model is to convolve the high resolution spectrum produced by SMART down to the lower resolution of the spectroscopic dataset. The exact form of the instrument convolution is flexible within SMARTER and the approach should depend on the data at hand. Throughout this work, retrievals of the lower resolution transmission spectra use a tophat convolution function to bin the high resolution model spectrum (sampled at 1 cm^{-1} wavenumber resolution) to the resolution of the binned data. Retrievals on the native high resolution ACE-FTS spectra use SMART’s internal triangular slit convolution function with a FWHM set to match that of the instru-

ment (0.02 cm^{-1}) and are oversampled by a factor of $2\times$ ($\Delta\nu = 0.00125 \text{ cm}^{-1}$) to allow the spectra to be interpolated onto the observed wavelength grid. Although the ACE-FTS instrument has a spectral response function that is best described by a sinc function (Bernath 2017), our initial fits using SMART’s pre-existing triangular slit convolution function showed excellent agreement at high resolution using the FWHM of the ACE-FTS instrument.

We note that although SMART has numerous features that are novel or rarely employed in exoplanet retrieval codes (e.g. ray tracing refraction, Monte Carlo scattering, aerosol phase functions, etc.), in this paper we use a baseline transmission forward model in SMARTER that, unless otherwise stated, does not include these features and is roughly equivalent in complexity to other retrieval codes in the literature. This serves to aid in the extension of our results retrieving on the empirical Earth spectrum to other retrieval codes used throughout the literature that use similar complexity. It also serves the goal of validating SMARTER prior to introducing additional complexity. These features will be explored in future work.

2.2.2. Inverse Model

We employ a multi-pronged inverse modeling approach similar to that of the CHIMERA retrieval model (Line et al. 2013, 2014; Kreidberg et al. 2015; Feng et al. 2016; Batalha et al. 2017a; Tremblay et al. 2020). Each inverse model uses Bayes’ Theorem to estimate the peak or characterize the shape of the posterior distribution. However, each method employs a different set of assumptions and numerical approaches that both affect the statistical robustness of the retrieved posteriors and the number of calls to the forward model required to converge. Three inverse models are currently available and can be used with any forward model within the SMARTER framework. These retrieval models are: Optimal Estimation (OE) using `scipy.optimize.minimize` and `scipy.optimize.curve_fit` (Virtanen et al. 2019; Virtanen et al. 2020), Nested Sampling (NS) using MULTINEST (Feroz & Hobson 2008; Feroz et al. 2009, 2013; Feroz et al. 2019) via the PYMULTINEST Python wrapper (Buchner et al. 2014) and DYNESTY (Speagle 2020), and Markov Chain Monte Carlo (MCMC) using EMCEE (Foreman-Mackey et al. 2013).

In this work we primarily use OE with `curve_fit` when errors are small/negligible to derive maximum likelihood estimates (MLE), and NS with DYNESTY to derive posterior distributions for cases with exoplanet relevant uncertainties. Nested sampling has been growing in popularity within the exoplanet atmospheric re-

trieval community, with most of the common retrieval codes now using it as their preferred inverse model (e.g. Benneke & Seager 2013; Line & Parmentier 2016; Lavie et al. 2017; Rocchetto et al. 2016; MacDonald & Madhusudhan 2017; Barstow et al. 2020). This broad adoption stems from its efficiency—requiring $\sim 10\times$ fewer forward model evaluations compared with traditional MCMC sampling—and its applicability in model selection problems, both of which are important for atmospheric retrievals. NS algorithms operate by iterating forward through nested shells of likelihood, progressively focusing on smaller and smaller regions of the prior volume. The procedure terminates once the marginal likelihood (evidence) is determined to some user-specified precision, for which we use the recommended value of 0.5 in log-evidence.

Table 1 provides the free parameters under consideration in our retrievals and their respective prior probabilities. All parameters have uninformative uniform priors. The retrievals using OE are initialized near their expected solutions based on the known vertical composition and temperature profile of the globally-averaged Earth.

2.3. Retrieval Experiments

We considered the atmospheric retrieval analysis of the Earth spectrum shown in Fig. 1 from a few different perspectives so as to (1) validate our retrieval model, (2) test common retrieval modeling assumptions, and (3) highlight different challenges and capabilities of exoplanet transmission spectroscopy.

Low Resolution Data—In our first set of experiments, we used SMARTER to fit the broad wavelength, low-resolution spectrum shown in the top panel of Fig. 1 (dark blue line). This experiment was designed to test the accuracy of the forward model at a modest spectral resolution, more representative of exoplanet data, over a broad wavelength range to include as many gas absorbers as possible.

High Resolution Data—In our second set of experiments, we analyzed the high-resolution spectrum and performed retrievals at the native resolution of the ACE-FTS instrument. Since the high resolution spectrum resolves most individual absorption lines at these wavelengths, the spectrum provides excellent sensitivity to a large range of atmospheric altitudes (see Fig. 4 in M&C19), which we investigate with our retrievals. In this case, we started by fitting the full $2 - 14 \mu\text{m}$ spectrum, and then we performed two narrow focused cases by individually fitting the $4.3 \mu\text{m}$ CO_2 band ($3.7 - 5 \mu\text{m}$) and the $6 \mu\text{m}$ window ($5.0 - 7.2 \mu\text{m}$). Fitting the

Table 1. Retrieval parameters and their respective priors.

Parameter	Model 1: “scaled profiles”			Model 2: “evenly-mixed”		
	Type	Initial ^a	Prior	Type	Initial	Prior
Temperature, T	fixed	—	—	linear isothermal ^b	255 K	$\mathcal{U}(100, 400)$
H ₂ O	linearly scaled profile	1.0	$\mathcal{U}(0, 100)$	log evenly-mixed	-3.12	$\mathcal{U}(-12, 0)$
CO ₂	linearly scaled profile	1.0	$\mathcal{U}(0, 100)$	log evenly-mixed	-3.42	$\mathcal{U}(-12, 0)$
O ₃	linearly scaled profile	1.0	$\mathcal{U}(0, 100)$	log evenly-mixed	-5.88	$\mathcal{U}(-12, 0)$
O ₂	linearly scaled profile	1.0	$\mathcal{U}(0, 100)$	log evenly-mixed	-0.67	$\mathcal{U}(-12, 0)$
N ₂	linearly scaled profile	1.0	$\mathcal{U}(0, 100)$	log evenly-mixed	-0.11	$\mathcal{U}(-12, 0)$
CH ₄	linearly scaled profile	1.0	$\mathcal{U}(0, 100)$	log evenly-mixed	-5.79	$\mathcal{U}(-12, 0)$
CO	linearly scaled profile	1.0	$\mathcal{U}(0, 100)$	log evenly-mixed	-6.80	$\mathcal{U}(-12, 0)$
NO ₂	linearly scaled profile	1.0	$\mathcal{U}(0, 100)$	log evenly-mixed	-8.50	$\mathcal{U}(-12, 0)$
N ₂ O	linearly scaled profile	1.0	$\mathcal{U}(0, 100)$	log evenly-mixed	-6.59	$\mathcal{U}(-12, 0)$
HNO ₃	linearly scaled profile	1.0	$\mathcal{U}(0, 100)$	log evenly-mixed	-8.34	$\mathcal{U}(-12, 0)$
CFC-11	linearly scaled profile	1.0	$\mathcal{U}(0, 100)$	log evenly-mixed	-9.64	$\mathcal{U}(-12, 0)$
CFC-12	linearly scaled profile	1.0	$\mathcal{U}(0, 100)$	log evenly-mixed	-9.29	$\mathcal{U}(-12, 0)$

NOTE— \mathcal{U} denotes a uniform prior distribution.

^aSee Figure 3 for the initial profile (subject to subsequent scaling) for each of these parameters.

^bWe also considered fixed TP profiles using Model 2.

3.7 – 5 μm wavelength range enables a more comprehensive assessment of the structure of the prominent CO₂ band and the bulk atmospheric N₂ abundance via N₂–N₂ CIA (Schwieterman et al. 2015b). Fitting the 5 – 7 μm wavelength range enables a focused glimpse into one of the largest H₂O absorption bands found in the M&C19 transmission spectrum, and a deeper dive into the O₂–O₂ and O₂–N₂ CIA bands recently highlighted by Fauchez et al. (2020). This experiment was designed to test the accuracy of our forward model at much higher spectral resolution than a typical exoplanet observation to further validate our model and to explore the limits of our 1D modeling approaches in the face of information rich transmission spectra of a known planet.

JWST Data—In our third set of experiments, we used the empirical Earth spectrum to generate synthetic JWST data using the NIRSpec and MIRI LRS instruments, respectively. In this case, we assumed that the exoplanet TRAPPIST-1e possesses Earth’s spectrum and applied a level of noise appropriate for 80 observed and stacked transits with each instrument. In this way, our mock observations with NIRSpec and MIRI LRS do not have the same level of uncertainty, but rather, they represent equivalent exposure times with two instruments that vary in wavelength range and spectral resolution. We note that the Earth’s atmosphere is not a good prediction for that of TRAPPIST-1e due primarily to the inconsistent evolutionary histories and photo-

chemistry with the stellar UV spectrum. However, this experiment is designed simply to have noise properties consistent with expectations for a long term JWST program. These JWST-relevant retrievals use the DYNesty nested sampling inverse model to derive full posterior distributions for the model parameters. This experiment was designed to provide the context within which to interpret all of our findings in the reference frame of near-term exoplanet observations with JWST.

3. RESULTS

Our results are organized into the following three investigations: (3.1) retrievals of the Earth’s low resolution transmission spectrum, (3.2) retrievals of the Earth’s high resolution transmission spectrum, and (3.3) retrievals of an Earth-analog TRAPPIST-1e spectrum as if it were observed with JWST.

3.1. Low Resolution Spectrum

3.1.1. Model 1

We begin by fitting the low resolution spectrum shown in dark blue in Fig. 1 using Model 1. Figure 5 shows our best-fitting solution to Earth’s full 2 – 14 μm transmission spectrum. We use semi-transparent colors to highlight the absorption features due to all molecules included in our model. Strong absorption features are clearly visible from H₂O, CO₂, and O₃, with smaller features due to CH₄, HNO₃, NO₂, N₂O, CFC-11, and CFC-12. We note that the N₂–N₂ CIA feature at 4.1

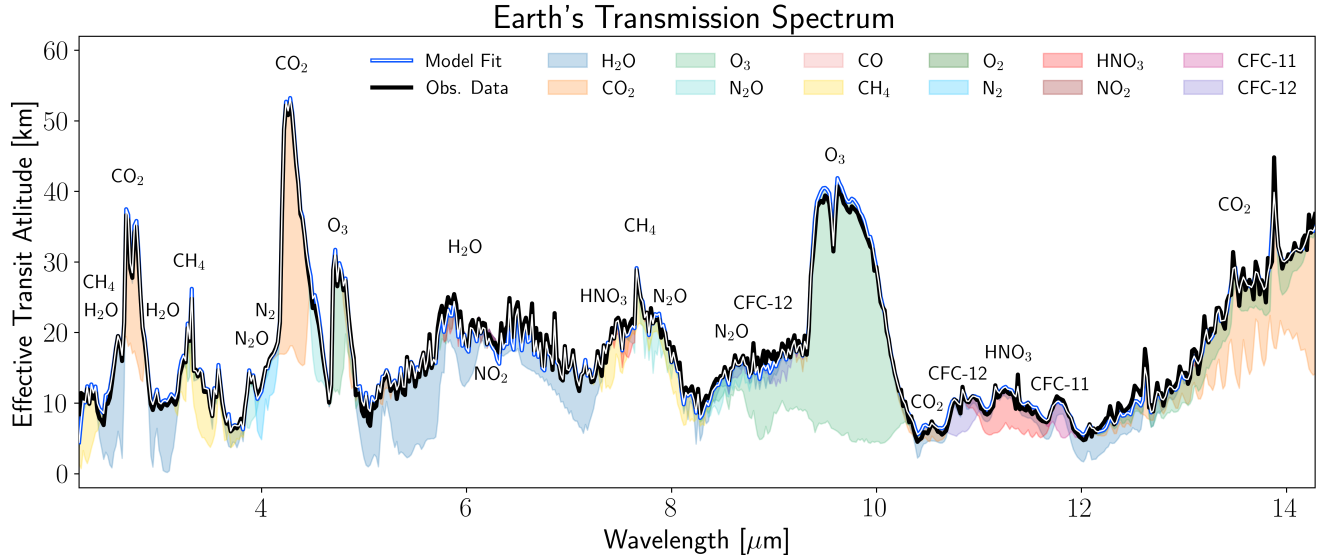


Figure 5. Earth’s observed cloud-free transit transmission spectrum from [Macdonald & Cowan \(2019\)](#) binned to a resolution of $\Delta\lambda = 0.02 \mu\text{m}$ and fit using SMARTER. The data are shown in black, the best-fitting model (Model 1) spectrum is shown in white and blue, and various colors are used to indicate each molecule’s contribution to the model spectrum. The most prominent features are due to CO_2 and O_3 , but a rich diversity of habitability indicators, biosignatures, and technosignatures are present.

μm is also visible (see [Schwieterman et al. 2015b](#)) and provides leverage to constrain the bulk atmospheric N_2 abundance. There is substantial agreement between our best-fitting model and the observed data. Our best-fitting spectrum has a mean percent error of 5.15% from the empirical transmission spectrum (with a maximum deviation of 5.45 km at 13.8 μm). We determined what the errors would need to be for our best fitting spectrum to have a reduced chi-squared of unity ($\chi_{red}^2 = 1$). This yielded a characteristic error of $z_{err} = 0.94$ km. Measurement errors larger than this characteristic modeling error result in our model being an excellent fit, while measurement errors smaller than this result in our model potentially requiring additional sophistication to better fit the spectrum. By using the planet and star radius, this characteristic error (or any altitude values) can be scaled to a typical exoplanet measurement precision via

$$\Delta F_{err} = \left(\frac{R_p + z_{err}}{R_s} \right)^2 - \left(\frac{R_p}{R_s} \right)^2, \quad (2)$$

which gives a mean uncertainty of about 0.024 ppm for an Earth-Sun exoplanet-analog transmission spectrum, or about 1.7 ppm for TRAPPIST-1e transiting TRAPPIST-1 ([Van Grootel et al. 2018](#)). These values are well below the noise floor of current and upcoming instruments ([Greene et al. 2016](#); [Stevenson & Fowler 2019](#); [Schlawin et al. 2021](#)). Exoplanet transmission spectra would need to be more precise than these ppm values for the deviations in our model fit with SMARTER to be considered significant.

Table 2 provides the mixing ratio scale factors retrieved for each molecule included in our low resolution fit in the column labeled “Model 1”. Most of the scale factors lie near unity, indicating good agreement with the expected mean composition of Earth’s atmosphere. The molecules with large absorption features tend to have retrieved abundances that deviate by less than 10–30% from the average Earth profiles. However, Earth’s atmosphere naturally exhibits spatial variability for the temperature structure and many of the gas profiles, which is likely a source of systematic error in the observed and hemispherically-averaged transmission spectrum. That is, the “true” atmospheric composition of Earth cannot be accurately expressed using a single set of 1D vertical profiles, which on their own overconstrains the solution. To aid in our comparisons, we identify Earth’s approximate spatial variability by calculating the percent deviation among the 1D profiles from the VPL Earth Model’s atmospheric structure database ([Robinson et al. 2010, 2011, 2014a](#); [Schwieterman et al. 2015a](#)). These values are reported for the majority of the molecules of interest in Table 3 for reference. For most molecules (e.g. H_2O , CO_2 , O_3 , N_2O , CH_4) our retrieved VMRs (with 1- σ Gaussian uncertainties) are consistent within the spatial variance seen across the globe. For example, we retrieved an O_3 VMR scale factor of 1.167 ± 0.094 times the expected mean profile, or $\sim 17\%$ higher, however O_3 profiles are known to vary spatially by about 25%. Thus, our retrieved O_3 result is consistent given both the uncertainties in the spectral fit and the systematic uncertainties that arise from fit-

Table 2. Retrieved parameters for Earth’s atmosphere from a fit to Earth’s low-resolution transmission spectrum

Parameters	Model 1	Model 2	
	Fixed TP	Fixed TP	Isothermal
T_0 [K]	—	—	192.3 ± 3.7
H ₂ O	0.72 ± 0.21	-5.177 ± 0.093	-4.69 ± 0.17
CO ₂	1.10 ± 0.14	-3.404 ± 0.060	-2.58 ± 0.14
O ₃	1.167 ± 0.094	-5.582 ± 0.068	-5.05 ± 0.16
N ₂ O	1.20 ± 0.31	-6.507 ± 0.027	-6.571 ± 0.044
CO	1.0 ± 1.4	-6.655 ± 0.061	-6.82 ± 0.10
CH ₄	1.18 ± 0.21	-5.77 ± 0.21	-5.26 ± 0.25
O ₂	0.94 ± 0.56	-4 ± 50	-11.9 ± 2.1
N ₂	1.0 ± 2.1	-0.32 ± 0.21	-0.31 ± 0.74
HNO ₃	2.06 ± 0.27	-7.935 ± 0.028	-7.655 ± 0.042
NO ₂	0.94 ± 0.65	-8.409 ± 0.041	-8.319 ± 0.069
CFC-11	3.83 ± 0.81	-9.150 ± 0.037	-10.122 ± 0.056
CFC-12	4.41 ± 0.69	-8.820 ± 0.031	-8.744 ± 0.044
MPE	5.15%	11.74%	11.60%
z_{err}	0.94 km	1.81 km	2.07 km

NOTE—Model 1 and Model 2 refer to the “scaled profiles” and “evenly-mixed” retrieval models, respectively. The expected Earth profiles for each molecule are displayed in Figure 3, with the approximate \log_{10} VMRs for Earth’s atmosphere given in Table 1. The best fitting spectrum for Model 1 is shown in Figure 5. The last two rows show the mean percentage error (MPE) and characteristic vertical uncertainty (z_{err}) for each spectral fit.

ting a 1D static atmospheric model to an observation of a time-varying 3D atmosphere. A similar result is found for H₂O where we retrieved a slightly lower than average VMR scale factor of 0.72 ± 0.21 , which is consistent within the 30% spatial and temporal variability exhibited across the Earth. We note that O₂, N₂, and CO have poorly constrained mixing ratios due to the lack of substantial absorption features across the studied wavelength range, although greater sensitivity to these molecules is achieved in our subsequent high resolution retrievals. For HNO₃, CFC-11, and CFC-12, we retrieve more than double the expected Earth average mixing ratios. These findings are consistent with those of Schreier et al. (2018) who also required elevated mixing ratios for these species in their comparisons to ACE-FTS transmission spectra relative to the mid-latitude mean profiles, likely due to increased concentrations of these gases at high northern and southern latitudes (Remedios et al. 2007).

Table 3. Approximate percent deviations in molecular species observed across Earth due to spatial and temporal variability

Molecule	Spatial/Temporal Deviations
H ₂ O	30%
CO ₂	<1%
O ₃	25%
N ₂ O	23%
CO	28%
CH ₄	34%
O ₂	<1%
N ₂	<1%

3.1.2. Model 2

We also fit the low resolution transmission spectrum using a forward model with evenly mixed gas profiles that exhibit no vertical structure (“Model 2”). Model 2 uses the \log_{10} volume mixing ratio of each gas as free parameters and is more representative of approaches applied to exoplanet atmospheric studies. We examine two treatments for the thermal structure: (1) fixing the TP profile at Earth’s characteristic spatially averaged vertical thermal structure and (2) fitting for a single-valued isothermal temperature structure.

Table 2 presents our retrieval findings for these evenly mixed Model 2 fits. Both evenly mixed models provide good fits to the low resolution Earth spectrum and although they are quantitatively worse than the scaled profiles model (“Model 1”) as seen by the mean percent error summary statistic, they are qualitatively similar to the spectrum shown in Figure 5. The isothermal model fit has a mean percentage error marginally lower than the fixed TP model, indicating that it fits the spectrum slightly better. This is due primarily to the additional flexibility afforded to the isothermal model, coupled to the fact that the mean Earth TP that we assumed need not be the correct nor optimal TP profile to fit this observed spectrum. However, the fixed TP model offers more precise and accurate results for most of the gases considered. For example, the molecules with the most prominent absorption features in the spectrum (see Fig. 5)—CO₂, O₃, H₂O, and CH₄—all had retrieved VMRs that were biased high when we fit for the isothermal temperature compared with our more accurate findings using a realistic fixed TP profile. Thus the slightly improved fit to the spectrum achieved with the isothermal

model came at the cost of inaccurate abundance constraints.

Our retrieved isothermal temperature of ~ 192 K is slightly lower than the mean temperature of the tropopause, which occurs near 0.1 bar, but is consistent with tropopause temperature measurements in the tropics (Hoinka 1999). For gases with substantial variability as a function of altitude, such as H_2O , O_3 , N_2O , CH_4 , and CO , our retrieved evenly mixed volume mixing ratios with the fixed TP model are consistent with true values of the vertical profiles at pressures near ~ 0.1 bar. Our H_2O constraint is consistent with the mean H_2O profile between 0.1 – 0.2 bar. Our O_3 constraint is consistent with the mean O_3 profile at ~ 0.04 bar. CH_4 and N_2O are consistent in the lower atmosphere at pressures higher than ~ 0.03 bar. CO is consistent at pressures between 0.02 – 0.05 bar.

3.1.3. Model 2 with Noise Added to the Spectrum

To further validate the retrieval part of SMARTER, we perform one final test on the low resolution, broad wavelength transmission spectrum with 10% random noise added to each spectral data point. We fit this noisy spectrum using Model 2 with SMARTER’s DYNESTY nested sampling implementation with the isothermal TP profile included as a free parameter. The use of 10% errors is motivated by the residual modeling errors for Model 2 in Table 2. Despite each spectral point having 10% uncertainties, the large number of data points results in the spectrum deviating from a flat line by $> 30\sigma$, indicating that the spectrum far exceeds current telescope capabilities for rocky exoplanets (e.g., Lustig-Yaeger & Fu et al. 2023; Moran et al. 2023). Therefore this retrieval with noise enables robust validation of the model using nested sampling.

Figure 6 shows the results of our low resolution retrieval on the 10% noise-added spectrum. Overall, the results are similar to the previous OE findings in that we reproduce the general characteristics of Earth’s atmosphere, including major absorbing species and the bulk N_2 atmospheric composition. However, the assumed uniform vertical composition introduces some biases, including overestimates of gases like CO_2 and CH_4 . The median retrieved spectral model has $\chi_{red}^2 = 1.94$. Residuals between the data and fit are relatively small for the bands from evenly-mixed CO_2 , but are more apparent for the bands of O_3 , especially near $9.6 \mu\text{m}$. This disparity indicates that ozone’s non-uniform vertical distribution and the resultant thermal inversion are important parameters to improve the fit for this panchromatic Earth transmission spectrum. N_2 is clearly favored as the bulk atmospheric constituent, but it is over-

estimated, while O_2 is not identified and the retrieval favors mixing ratios $< 10\%$ at 2σ . The absolute precision on each retrieved parameter is not particularly meaningful as it depends on our choice of data errors, but the relative precision between each atmospheric gas indicates their prominence in the spectrum. In this wavelength range, our most challenging gases to retrieve are O_2 , CO , and NO_2 . Although SMARTER began its nested sampling retrieval with broad and uniform priors (Table 1) it converged to the correct atmospheric composition of Earth (modulo the aforementioned model limitations), demonstrating the validity of the retrieval model on a high quality transmission spectrum of a habitable and inhabited planet.

3.2. High Resolution Spectrum

We now shift to examine the Earth transmission spectrum at the high native spectral resolution ($R = 100,000$ at $5 \mu\text{m}$) of the occultation-derived measurements. To simulate the high-resolution spectrum with our forward model, we used SMART’s internal triangular slit function with the appropriate FWHM for the ACE-FTS instrument (0.02 cm^{-1}). We output spectra on a wavenumber grid with a sampling resolution of 0.00125 cm^{-1} , which oversamples the data by a factor of 2. We then interpolated the model spectrum onto the observed data wavelength grid.

We performed three separate assessments using data covering different wavelength ranges. First, we fit the full 2–14 μm wavelength range. Second, we focus on the more narrow 3.7–5 μm wavelength range to specifically isolate and examine the 4.3 μm CO_2 band. Third, we focus on the 5–7.2 μm wavelength range to isolate the strong 6 μm H_2O band and explore the overlapping contributions from O_2 and N_2 CIA.

3.2.1. Full Spectrum: 2 – 14 μm

Figure 7 shows our best fit model to the high resolution Earth transmission spectrum over the full 2–14 μm wavelength range using Model 1 and assuming the mean Earth TP profile. The zoomed panels highlight the 3.3 μm CH_4 band in the NIR (left column of subplots) and the 9–12 μm MIR range that contains significant absorption features from O_3 , CO_2 ($\sim 10.5 \mu\text{m}$), CFC-12, HNO_3 , and CFC-11 (right column of subplots).

Table 4 shows the retrieval results for our fit to the full wavelength range for the high resolution transmission spectrum using Model 1 with a variety of different Earth TP profiles. In general, the VMR scale factors reside near unity and the fits to the spectrum are good with average errors on the fits $< 10\%$. The reported 1σ errors on the retrieved parameters are much smaller than those from our fits to the low resolution spectrum,

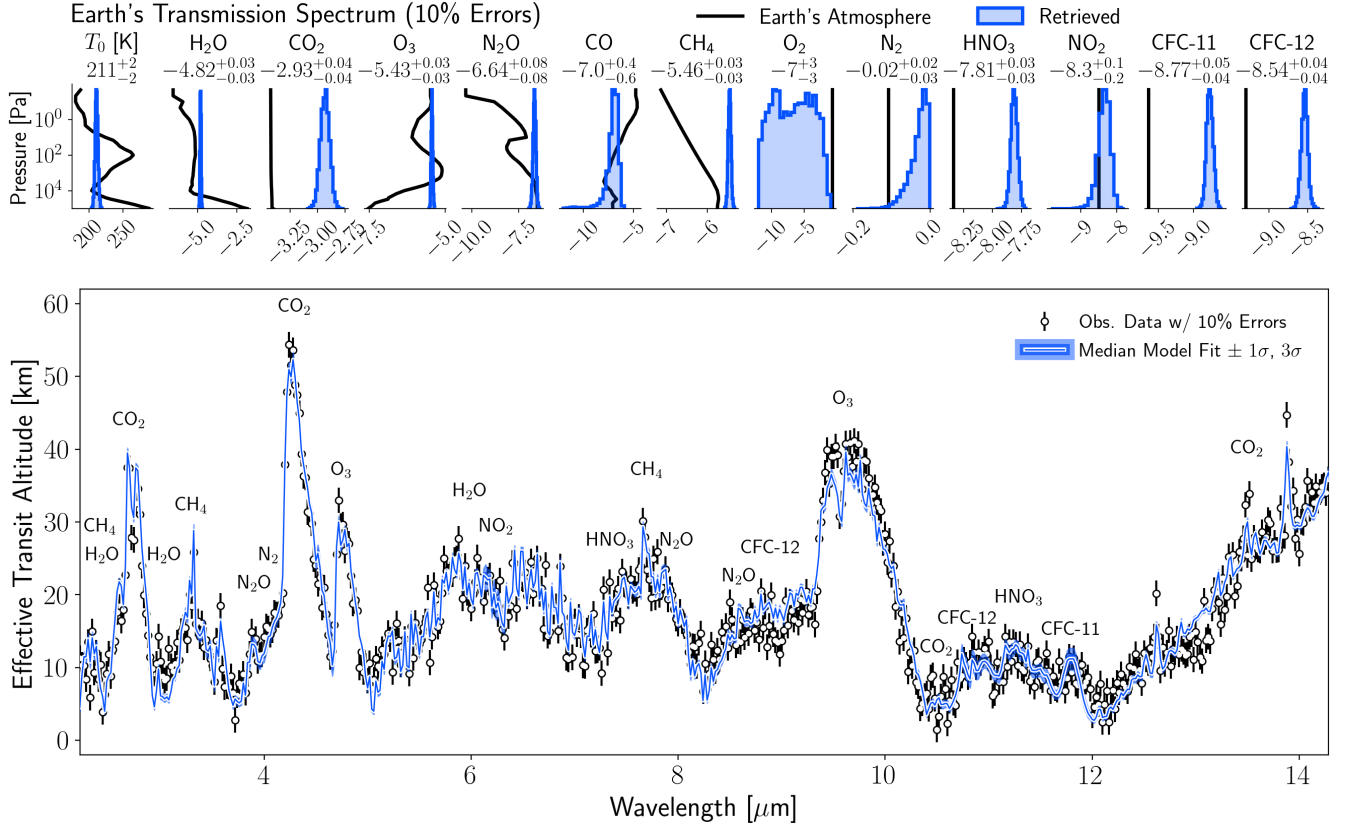


Figure 6. Retrieval results on Earth’s observed cloud-free transit transmission spectrum binned to a resolution of $\Delta\lambda = 0.02 \mu\text{m}$, with 10% random noise added, and fit using the DYNESTY nested sampling algorithm. The upper set of panels show 1D posterior histograms (blue) for each model parameter compared to the respective “true” atmospheric profiles from Figure 3. The median and 1σ intervals are listed above each panel. The lower panel shows the spectral data (black with uncertainties) and the median retrieved model spectrum (white and blue) surrounded by 1σ and 3σ credibility envelopes (often thinner than the median model line width).

which increases the significance of the deviations from the Earth averaged profiles. The deviations from unity still largely fall within the range of spatial and temporal variability reported in Table 3. For each molecule, we see that the retrieved VMR scale factors exhibit greater variance with the choice of TP profile than the uncertainties on the parameters themselves. This indicates an important relationship between the TP profile and the ability to accurately retrieve gas abundances. However, an interesting extension of this is seen in Table 4 where different TP profiles yield retrieved gas VMRs that are most consistent with the Earth averaged profiles for different molecules. For example, the 19° latitude TP profile yields the most consistent H₂O retrieval, the 41° latitude TP profile yields the most consistent CO₂ retrieval, and the 0° latitude TP profile yields the most consistent O₃ retrieval. Thus, we may not have considered the optimal TP profile or there may not be an optimal profile, but rather the transmission spectrum

may bear the markings of multiple TP profiles that exist simultaneously at different locations.

Figure 8 compares our retrieved CO₂ concentration to the temporal evolution of CO₂ that was reported using the same ACE-FTS measurements during the first few years of data collection. The nature of the empirical transmission spectrum from M&C19 being vertically integrated, spatially integrated, and temporally integrated precludes such an in-depth temporal study as that performed by Foucher et al. (2011). Nonetheless, our findings are statistically consistent with the results from Foucher et al. (2011) for CO₂. The exact cause of the remaining deviation from the expected value could be the result of one or more complicating effects. Since ACE-FTS continues to operate, it is possible that the M&C19 spectrum contains measurements beyond 2008, which would agree with our slightly higher CO₂ result considering the mean growth rate for CO₂, however, it is not clear from M&C19 exactly which years were used for the construction of the transmission spectrum. We also cannot rule out non-local thermodynamic equilib-

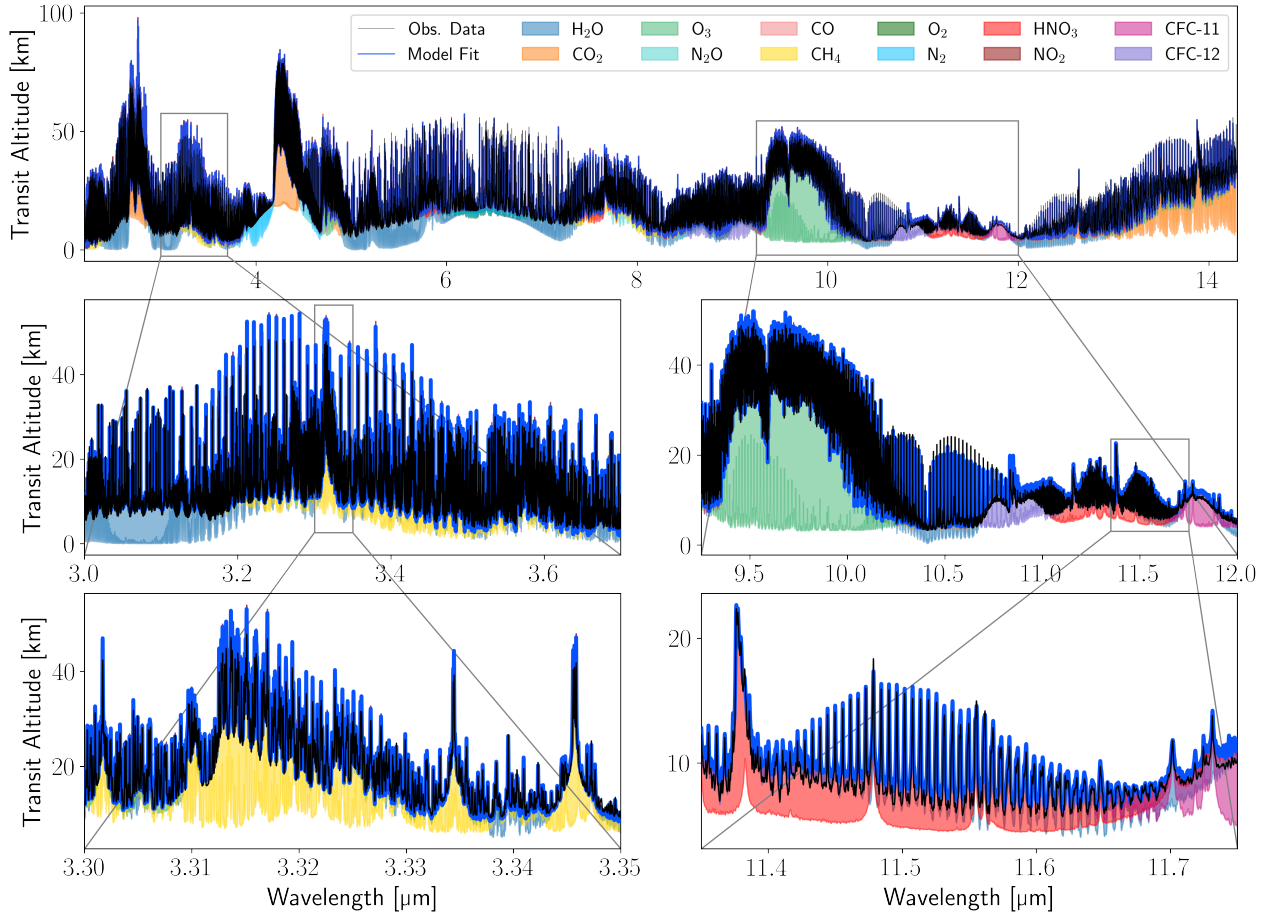


Figure 7. Best fit model of Earth’s high resolution transmission spectrum in the full 2 – 14 μm wavelength range using the mean Earth TP profile. The data are shown in black, the best-fitting model spectrum is shown in blue, and various colors are used to indicate each molecule’s contribution to the model spectrum.

rium (NLTE) effects in the upper atmosphere that could be causing minor residuals seen in the cores of the CO_2 lines, since NLTE effects are neglected in our model. Finally, systematic errors from the instrument could also explain the slight discrepancy, as discussed in more detail in Section 4.

Table 5 lists the retrieved atmospheric parameters using the evenly mixed atmospheric composition model (Model 2) for one retrieval with a free isothermal TP profile and a set of retrievals with the TP profile fixed at the various profiles shown in Figure 4. The model with the free isothermal TP profile provides a better fit to the data (15.21% error) compared to the models with fixed TP profiles (21.3% error on average), which show minimal variation between their results. However, the isothermal model retrieves biased results that systematically overestimate the true gas mixing ratios, similar to our results at low resolution. For example, the isothermal model retrieves a CO_2 VMR of 2032 ppm while the retrievals with fixed TP profiles find CO_2 between 296 ppm and 500 ppm—values that are much more consis-

tent with Earth’s known CO_2 (e.g., Figure 8). Compared to the results shown using the scaled profiles retrieval model (Model 1), the evenly mixed model (Model 2) provides worse fits to the high resolution spectrum and the resulting gas mixing ratios exhibit less variance when switching between different fixed TP profiles.

3.2.2. *Narrow Focus: 3.7 – 5 μm*

We now narrow our focus to the 3.7 – 5 μm wavelength range. This spectral interval is particularly notable for the strong 4.3 μm CO_2 band, the 4.7 μm O_3 band, and the 4.2 μm $\text{N}_2\text{--N}_2$ CIA band (Schwieterman et al. 2015b).

Figure 9 shows our best fit spectrum using Model 1 in the 3.7 – 5 μm wavelength range compared to the Earth observations. The middle zoomed inset reveals the molecules that are responsible for the majority of the absorption features in this spectral range: CO_2 , O_3 , N_2 , N_2O , and H_2O . The bottom left panel highlights the individual CO_2 lines within the 4.2 μm CO_2 band, which are well fit by our model. The bottom right panel

Table 4. Retrieved molecule VMR scale factors from OE fits to Earth’s high-resolution transmission spectrum in the 2 – 14 μm wavelength range

Parameters	avg	lat=0°	lat=19°	lat=41°	lat=66°	cold
H ₂ O	1.3082 ± 0.0061	0.8794 ± 0.0053	1.0411 ± 0.0053	1.6548 ± 0.0073	2.2986 ± 0.0094	2.2324 ± 0.0095
CO ₂	1.0213 ± 0.0038	0.9373 ± 0.0039	0.9343 ± 0.0037	1.0147 ± 0.0037	1.2375 ± 0.0045	1.3753 ± 0.0052
O ₃	1.1562 ± 0.0036	1.0616 ± 0.0036	1.0934 ± 0.0036	1.2271 ± 0.0038	1.3155 ± 0.0040	1.5039 ± 0.0047
N ₂ O	0.9574 ± 0.0067	0.8933 ± 0.0072	0.9403 ± 0.0070	1.1024 ± 0.0073	1.2669 ± 0.0081	1.4247 ± 0.0094
CO	0.751 ± 0.022	0.518 ± 0.022	0.638 ± 0.022	0.433 ± 0.019	0.703 ± 0.021	0.878 ± 0.022
CH ₄	1.2221 ± 0.0039	1.0400 ± 0.0038	1.0968 ± 0.0038	1.2268 ± 0.0039	1.4180 ± 0.0044	1.5784 ± 0.0050
O ₂	0.692 ± 0.012	0.746 ± 0.014	0.637 ± 0.013	0.527 ± 0.012	0.774 ± 0.013	0.947 ± 0.014
N ₂	2.8 ± 0.0	3.0 ± 0.0	3.1 ± 0.0	3.9 ± 0.0	1.4 ± 0.0	1.7 ± 0.0
HNO ₃	2.329 ± 0.016	2.412 ± 0.018	2.338 ± 0.016	3.127 ± 0.020	2.683 ± 0.018	2.800 ± 0.019
NO ₂	0.738 ± 0.015	0.730 ± 0.016	0.632 ± 0.015	0.810 ± 0.015	0.774 ± 0.016	0.914 ± 0.017
CFC-11	6.090 ± 0.074	3.761 ± 0.061	4.249 ± 0.060	4.549 ± 0.059	7.763 ± 0.084	6.942 ± 0.080
CFC-12	7.222 ± 0.053	4.900 ± 0.044	5.455 ± 0.045	5.323 ± 0.043	6.640 ± 0.049	6.964 ± 0.053
MPE	8.28%	10.91%	9.42%	8.03%	7.66%	8.06%
z_{err}	1.60 km	1.73 km	1.66 km	1.60 km	1.58 km	1.63 km

NOTE—Columns are labeled in reference to the fixed TP profiles shown in Figure 4. The fiducial Earth profiles for each molecule are displayed in Figure 3. The last two rows show the mean percentage error (MPE) and characteristic vertical uncertainty (z_{err}) for each spectral fit.

Table 5. Retrieved parameters for Earth’s atmosphere from a fit to Earth’s high-resolution transmission spectrum in the 2 – 14 μm wavelength range using an evenly mixed atmospheric model (Model 2)

Parameters	Isothermal TP	avg	lat=0°	lat=19°	lat=41°	lat=66°	cold
T_0 [K]	191.912 ± 0.066	—	—	—	—	—	—
H ₂ O	−4.6893 ± 0.0029	−5.1769 ± 0.0026	−5.2761 ± 0.0030	−5.0664 ± 0.0024	−5.1771 ± 0.0028	−5.1046 ± 0.0026	−4.9887 ± 0.0025
CO ₂	−2.6921 ± 0.0023	−3.4953 ± 0.0015	−3.5284 ± 0.0015	−3.5420 ± 0.0016	−3.5062 ± 0.0015	−3.4084 ± 0.0015	−3.3016 ± 0.0014
O ₃	−5.0999 ± 0.0036	−5.4944 ± 0.0029	−5.5608 ± 0.0030	−5.4291 ± 0.0028	−5.5077 ± 0.0029	−5.4465 ± 0.0029	−5.3241 ± 0.0027
N ₂ O	−6.05010 ± 0.00067	−6.53024 ± 0.00062	−6.52583 ± 0.00062	−6.52594 ± 0.00063	−6.52506 ± 0.00062	−6.42177 ± 0.00063	−6.44467 ± 0.00063
CO	−6.5242 ± 0.0015	−6.7230 ± 0.0014	−6.7446 ± 0.0013	−6.7151 ± 0.0014	−6.7156 ± 0.0014	−6.6341 ± 0.0014	−6.6364 ± 0.0014
CH ₄	−5.5228 ± 0.0034	−5.8521 ± 0.0031	−5.8930 ± 0.0031	−5.9399 ± 0.0032	−5.8516 ± 0.0031	−5.8977 ± 0.0033	−5.8493 ± 0.0032
O ₂	−1.868 ± 0.027	−1.382 ± 0.026	−0.9128 ± 0.0092	−1.301 ± 0.025	−1.048 ± 0.013	−1.410 ± 0.027	−1.219 ± 0.018
N ₂	−0.0057 ± 0.0043	−0.1198 ± 0.0026	−0.1934 ± 0.0029	−0.0717 ± 0.0023	−0.1261 ± 0.0026	−0.0058 ± 0.0024	−0.0168 ± 0.0025
HNO ₃	−7.6634 ± 0.0011	−8.2517 ± 0.0012	−8.2489 ± 0.0012	−8.2791 ± 0.0012	−8.2519 ± 0.0012	−8.2210 ± 0.0012	−8.2354 ± 0.0011
NO ₂	−7.9282 ± 0.0012	−8.6241 ± 0.0013	−8.6665 ± 0.0014	−8.6294 ± 0.0013	−8.6324 ± 0.0014	−8.5310 ± 0.0013	−8.5662 ± 0.0013
CFC-11	−9.5848 ± 0.0019	−9.2770 ± 0.0018	−9.2829 ± 0.0019	−9.2844 ± 0.0019	−9.2671 ± 0.0018	−9.2845 ± 0.0018	−9.2624 ± 0.0018
CFC-12	−8.9630 ± 0.0017	−9.2019 ± 0.0018	−9.2179 ± 0.0018	−9.2155 ± 0.0018	−9.1963 ± 0.0018	−9.1698 ± 0.0018	−9.1775 ± 0.0017
MPE	15.21%	21.19%	21.76%	21.37%	21.38%	21.84%	20.71%
z_{err}	2.42 km	2.90 km	2.93 km	2.92 km	2.92 km	2.95 km	2.87 km

NOTE—Columns with fixed TP profiles are labeled in reference to those shown in Figure 4. The expected Earth profiles for each molecule are displayed in Figure 3, with the approximate \log_{10} VMRs for Earth’s atmosphere given in Table 1. The last two rows show the mean percentage error (MPE) and characteristic vertical uncertainty (z_{err}) for each spectral fit.

highlights a small region of the 4.7 μm O₃ band and how it overlaps with the 4.6 μm CO band. This CO band is much more subtle than the O₃ band, but it can be visually identified by the series of relatively strong lines seen in the middle panel of Figure 9 that span from around 4.55–4.8 μm , and include the two strongest lines contained in the bottom right panel. Across the entire

2 – 14 μm transmission spectrum, this is the strongest CO band.

Table 6 displays the retrieval results for Model 1 using data covering only the 3.7 – 5 μm wavelength range of interest. For the aforementioned molecules with strong features in this narrow wavelength range, our inferred VMRs tend to be within 10% of the global Earth averages. However, like our results across the full wavelength

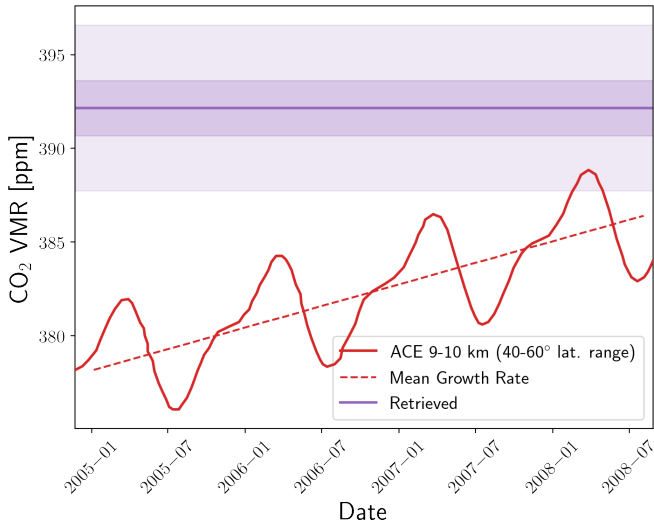


Figure 8. Retrieved CO_2 VMR from the high resolution full wavelength spectrum compared to the temporal evolution of the CO_2 concentration retrieved from ACE as reported in Foucher et al. (2011). The purple line shows our retrieved CO_2 VMR with dark and light shading to indicate the 1σ and 3σ credible intervals, respectively, from our model fixed at the average Earth TP profile. The agreement is quite good considering that the transmission spectrum fit using our model is vertically integrated over the atmospheric column, spatially integrated over the entire globe, and temporally integrated over many years of SCISAT mission operation.

range, these results exhibit sensitivity to the assumed TP profile. Compared to the full wavelength range, focusing on this narrow range enables a more accurate retrieval of N_2 . O_2 , HNO_3 , NO_2 , CFC-11, and CFC-12 have no features in this wavelength range and are not constrained by these retrievals.

Table 7 shows the retrieval results for the evenly mixed atmospheric model (Model 2) in the $3.7 - 5 \mu\text{m}$ wavelength range. Unlike the results seen across the full $2 - 14 \mu\text{m}$ range, in this case, the isothermal model provides a marginally worse fit to the data (10.44% error) compared to the retrievals using physically-motivated fixed TP profiles (9.92% error on average). The retrieved isothermal temperature of $\sim 246 \text{ K}$ is much higher than what we found using the full wavelength range. This may be a consequence of the strong CO_2 band that dominates this wavelength range and causes absorption in the warm upper stratosphere. The evenly mixed VMRs also appear to be less biased when the isothermal TP profile is used compared to the full wavelength range.

3.2.3. Narrow Focus: $5 - 7.2 \mu\text{m}$

We now focus exclusively on the $6 \mu\text{m}$ region ($5 - 7.2 \mu\text{m}$) to delve deeper into H_2O , O_2 , and N_2 . Table 8 displays the retrieval results from our fit to the high resolu-

tion transmission spectrum using Model 1 with various different TP and water vertical profiles. In general, the fits to the high resolution data are very good with model deviations under 10%. Again, no single vertical profile enables an accurate VMR retrieval of all the gases; instead, some profiles provide more accurate results for specific gases. The average Earth profile yields the most accurate retrieval of the CO_2 and O_3 abundances, but not the O_2 and N_2 abundances. The high latitude/cold profiles provide a more accurate assessment of O_2 and N_2 , but retrieves a CO_2 abundance that exceeds the current Earth value by a factor of ~ 2 . Furthermore, the higher latitude/cold profiles provide better fits to the entire $6 \mu\text{m}$ spectral range than the lower latitude profiles.

Figure 10 shows our best-fitting model (Model 1) in the $6 \mu\text{m}$ region using the 66° latitude TP and water profiles. As shown in Table 8, the 66° latitude profiles provided the overall best fit to the data in the spectral region and the most accurate inferred VMR for O_2 and N_2 , which we will examine more closely. In the top two panels it is difficult to discern the differences between the model (in blue) and the data (in black) because both lines plot on top of one another. The bottom panels of Fig. 10 zoom into a narrow enough region to see small deviations. These lower two panels highlight the contribution from various line and continuum absorbers. In the third panel, there are several well-resolved H_2O lines that make up the $6 \mu\text{m}$ absorption band and span approximately 50 km in absorbing radius from the continuum to their cores. The fourth panel zooms into a region between H_2O lines where the opacity is low and contributions to the continuum are visible from $\text{O}_2 - \text{N}_2$ CIA, $\text{O}_2 - \text{O}_2$ CIA, and H_2O . Note that the green shading for O_2 shows the combined absorption due to $\text{O}_2 - \text{O}_2$ CIA and $\text{O}_2 - \text{N}_2$ CIA and therefore the absorption contribution from $\text{O}_2 - \text{O}_2$ CIA alone is identified by the green shading that extends below the purple shading for $\text{O}_2 - \text{N}_2$. In this region, there are also subtle absorption features due to HNO_3 and CH_4 . Between $5 - 7.2 \mu\text{m}$ this best-fitting spectrum has a 3.41% percent deviation on average from the empirical transmission spectrum and a characteristic error of $z_{err} = 0.91 \text{ km}$.

At high spectral resolution, the continuum in the $6 \mu\text{m}$ range provides a compelling window through which to study the lower atmosphere between H_2O lines, but it appears to be home to a complex degeneracy between multiple competing continuum absorbers (Figure 10). The continuum between $5 - 7 \mu\text{m}$ proved to be one of the most challenging spectral regions to fit in the entire $2 - 14 \mu\text{m}$ Earth transmission spectrum from M&C19. Specifically, the residuals that caused the globally aver-

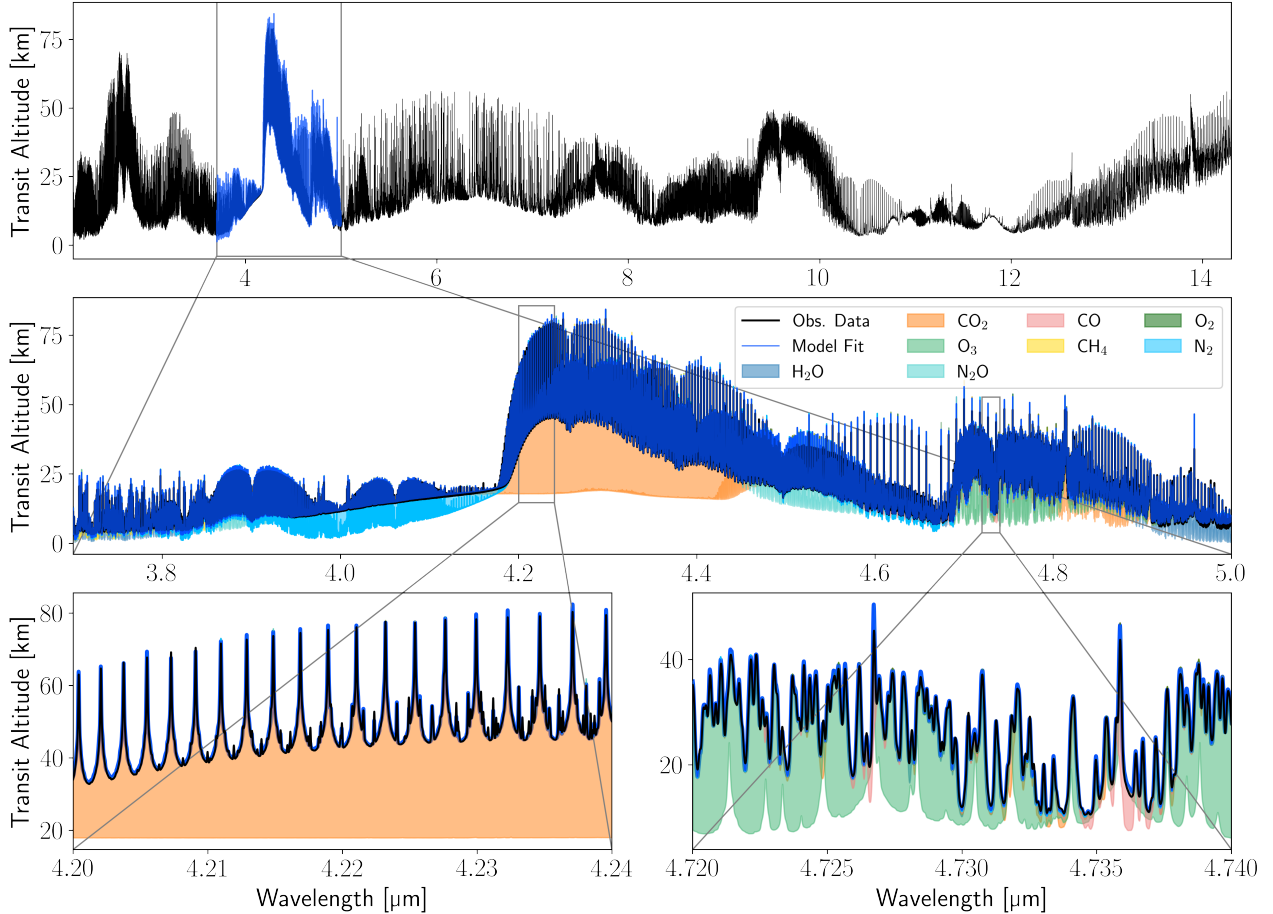


Figure 9. Best fit model of Earth’s high resolution transmission spectrum in the 3.7 – 5 μm wavelength range using the mean Earth TP profile. The data are shown in black, the best-fitting model spectrum is shown in blue, and various colors are used to indicate each molecule’s contribution to the model spectrum.

aged, 0° latitude, and 19° latitude TP/water profiles to exhibit larger fitting errors, arose primarily from poor fits to the H_2O continuum between 5 – 5.7 μm and beyond 6.5 μm . Although the “cold” and 61° latitude profiles provided the best fits to the spectral continuum, they resulted in anomalously high CO_2 , H_2O , and O_3 VMRs. H_2O and O_3 exhibit spatial variability, but since CO_2 effectively does not, these deviations from the known values further highlight a degeneracy that can bias retrievals away from the true result while still yielding an excellent fit to the observations. The lower two panels of Figure 10 show how the spectral continuum is produced through a combination of absorption processes, including the 6 μm H_2O band continuum, O_2 – O_2 CIA, and O_2 – N_2 CIA. Since the choice of vertical temperature and H_2O profiles strongly affected the retrieved O_2 and N_2 VMR (see Table 8), we infer that there are complex degeneracies between the vertical TP structure, H_2O profile, and the VMRs of O_2 and N_2 . For Earth, we can hold many of these parameters fixed to break such a degeneracy, but for future exoplanet observations, de-

generacies between the vertical thermal structure and mixing ratio profiles may be quite challenging to diagnose and overcome when little or no prior information is known.

Table 9 lists the results from our evenly mixed retrievals in the 5 – 7 μm range using Model 2 with an isothermal TP profile (column 1) and the assortment of fixed TP profiles (columns 2-7). Similar to our previous results, the evenly mixed models are not able to provide as good of fits to the Earth observations as the scaled profiles that assume an approximately correct 1D vertical structure (results shown in Table 8). We report mean percentage errors on the fits of 14.68% and 14.38% for the mean TP profile and isothermal fitted models, respectively. Again we see that the flexibility of the isothermal model provides a marginally better fit to the data than a realistic, but fixed, TP profile, however it has a propensity to retrieve biased gas VMRs. This bias is exemplified well by the CO_2 VMR, which is over estimated by an order of magnitude by the isothermal model compared to all of our results with various fixed

Table 6. Retrieved molecule VMR scale factors from OE fits to Earth’s high-resolution transmission spectrum in the 3.7 – 5 μm wavelength range

Parameters	avg	lat=0°	lat=19°	lat=41°	lat=66°	cold
H ₂ O	1.064 ± 0.018	0.573 ± 0.014	0.712 ± 0.015	1.332 ± 0.023	2.827 ± 0.046	4.186 ± 0.066
CO ₂	1.1032 ± 0.0038	1.0040 ± 0.0035	1.0125 ± 0.0035	1.1032 ± 0.0038	1.3436 ± 0.0047	1.5793 ± 0.0057
O ₃	1.0744 ± 0.0042	1.0122 ± 0.0040	1.0368 ± 0.0040	1.0902 ± 0.0043	1.1900 ± 0.0048	1.2851 ± 0.0054
N ₂ O	0.9010 ± 0.0059	0.8396 ± 0.0059	0.8543 ± 0.0057	0.9035 ± 0.0059	0.9930 ± 0.0060	1.0630 ± 0.0066
CO	0.941 ± 0.016	0.783 ± 0.015	0.735 ± 0.015	0.937 ± 0.016	0.824 ± 0.016	0.845 ± 0.017
CH ₄	1.441 ± 0.011	1.2269 ± 0.0096	1.3147 ± 0.0097	1.467 ± 0.011	1.637 ± 0.012	1.609 ± 0.012
O ₂	1.82 ± 0.20	2.78 ± 0.31	3.71 ± 0.41	1.80 ± 0.25	4.880 ± 0.000	3.25 ± 0.37
N ₂	1.172 ± 0.083	1.088 ± 0.047	1.104 ± 0.050	1.176 ± 0.082	1.439 ± 0.000	1.311 ± 0.000
MPE	4.50%	4.84%	4.46%	4.44%	4.45%	4.44%
z_{err}	0.89 km	0.90 km	0.88 km	0.90 km	0.91 km	0.93 km

NOTE—HNO₃, NO₂, CFC-11, and CFC-12 were not constrained and are therefore omitted from the table. Columns are labeled in reference to the fixed TP profiles shown in Figure 4. The fiducial Earth profiles for each molecule are displayed in Figure 3. The last two rows show the mean percentage error (MPE) and characteristic vertical uncertainty (z_{err}) for each spectral fit.

Table 7. Retrieved parameters for Earth’s atmosphere from a fit to Earth’s high-resolution transmission spectrum in the 3.7 – 5 μm wavelength range using an evenly mixed atmospheric model (Model 2)

Parameters	Isothermal TP	avg	lat=0°	lat=19°	lat=41°	lat=66°	cold
T_0 [K]	245.66 ± 0.17	—	—	—	—	—	—
H ₂ O	−4.406 ± 0.015	−4.391 ± 0.014	−5.060 ± 0.026	−4.612 ± 0.017	−4.382 ± 0.014	−4.393 ± 0.015	−4.429 ± 0.016
CO ₂	−3.6906 ± 0.0047	−3.4064 ± 0.0011	−3.4567 ± 0.0012	−3.4458 ± 0.0011	−3.4095 ± 0.0012	−3.3167 ± 0.0012	−3.2327 ± 0.0011
O ₃	−5.6016 ± 0.0066	−5.4823 ± 0.0047	−5.4785 ± 0.0046	−5.4864 ± 0.0045	−5.4666 ± 0.0047	−5.4286 ± 0.0048	−5.4087 ± 0.0047
N ₂ O	−6.6937 ± 0.0013	−6.60102 ± 0.00094	−6.63791 ± 0.00093	−6.64024 ± 0.00092	−6.59063 ± 0.00094	−6.52346 ± 0.00096	−6.50035 ± 0.00096
CO	−7.1207 ± 0.0017	−7.4039 ± 0.0017	−7.3059 ± 0.0016	−7.4493 ± 0.0016	−7.4174 ± 0.0017	−7.3946 ± 0.0017	−7.6562 ± 0.0018
CH ₄	−5.608 ± 0.011	−5.736 ± 0.011	−5.759 ± 0.011	−5.721 ± 0.010	−5.715 ± 0.011	−5.688 ± 0.011	−5.651 ± 0.011
O ₂	−0.019 ± 0.032	−0.68 ± 0.10	−0.675 ± 0.023	−0.699 ± 0.019	−0.689 ± 0.079	−0.691 ± 0.019	−0.729 ± 0.019
N ₂	−0.0564 ± 0.0018	−0.0926 ± 0.0019	−0.0984 ± 0.0018	−0.0922 ± 0.0018	−0.0877 ± 0.0019	−0.0814 ± 0.0021	−0.0721 ± 0.0022
MPE	10.44%	9.77%	10.24%	9.57%	9.72%	10.20%	10.03%
z_{err}	1.96 km	1.72 km	1.69 km	1.66 km	1.73 km	1.77 km	1.74 km

NOTE—HNO₃, NO₂, CFC-11, and CFC-12 were not constrained and are therefore omitted from the table. Columns with fixed TP profiles are labeled in reference to those shown in Figure 4. The expected Earth profiles for each molecule are displayed in Figure 3, with the approximate log₁₀ VMRs for Earth’s atmosphere given in Table 1. The last two rows show the mean percentage error (MPE) and characteristic vertical uncertainty (z_{err}) for each spectral fit.

TP profiles. We retrieved an isothermal temperature of 203.02 ± 0.30 K, which agrees well with the average Earth tropopause temperature, but varies appreciably from the isothermal temperatures inferred using other portions of the spectrum. The fact that we retrieved different isothermal temperatures in each of the spectral regions considered at high resolution illuminates the sensitivity of the broad wavelength transmission spectrum to vertical temperature structure.

As an addendum to the investigations presented here, we performed a brief investigation on the impact of atmospheric refraction in our radiative transfer modeling. Appendix A demonstrates that a small systematic effect is present due to the increase in optical path

length caused by refraction. This effect increases towards the lower atmosphere where the density is higher. While some biases in the abundance retrievals could be attributed to neglecting refraction, these effects are smaller than those exhibited by different TP profiles and vertical modeling assumptions.

3.3. Synthetic JWST Observations

We now consider the Earth’s transmission spectrum as if it were observed with JWST. Until this point, we have fit the empirical Earth spectrum in units of kilometers altitude above the solid surface; now, we transform the observations into transit depths, assuming that TRAPPIST-1e exhibits this exact spectrum. We define

Table 8. Retrieved molecule VMR scale factors from OE fits to Earth’s high-resolution transmission spectrum in the 5 – 7.2 μm wavelength range

Parameters	avg	lat=0°	lat=19°	lat=41°	lat=66°	cold
H ₂ O	1.5556 ± 0.0086	1.266 ± 0.011	1.3751 ± 0.0099	1.5820 ± 0.0083	1.9575 ± 0.0095	2.246 ± 0.011
CO ₂	1.034 ± 0.014	0.737 ± 0.020	0.734 ± 0.016	1.085 ± 0.013	1.782 ± 0.017	1.926 ± 0.019
O ₃	0.9411 ± 0.0090	0.654 ± 0.013	0.703 ± 0.011	1.1958 ± 0.0094	1.558 ± 0.011	1.653 ± 0.012
N ₂ O	0.837 ± 0.039	0.723 ± 0.062	0.534 ± 0.046	0.828 ± 0.034	1.772 ± 0.050	1.707 ± 0.050
CO	0.0 ± 1.4	16.0 ± 5.9	2.8 ± 3.2	0.5 ± 1.1	1.0 ± 1.1	14.4 ± 2.9
CH ₄	1.083 ± 0.024	0.883 ± 0.033	0.975 ± 0.028	1.299 ± 0.024	1.532 ± 0.027	1.435 ± 0.027
O ₂	0.5775 ± 0.0099	0.639 ± 0.036	0.468 ± 0.012	1.332 ± 0.080	0.978 ± 0.023	0.808 ± 0.010
N ₂	3.848 ± 0.000	0.77 ± 0.37	1.653 ± 0.000	0.28 ± 0.17	0.97 ± 0.26	2.412 ± 0.000
HNO ₃	4.348 ± 0.036	4.613 ± 0.057	4.405 ± 0.046	4.081 ± 0.032	4.085 ± 0.033	3.529 ± 0.031
NO ₂	0.749 ± 0.012	0.807 ± 0.019	0.798 ± 0.016	0.753 ± 0.011	0.709 ± 0.012	0.753 ± 0.012
MPE	4.87%	9.00%	7.01%	3.87%	3.41%	3.76%
z_{err}	1.00 km	1.51 km	1.26 km	0.92 km	0.91 km	0.93 km

NOTE—CFC-11 and CFC-12 were not constrained and are therefore omitted from the table. Columns are labeled in reference to the fixed TP profiles shown in Figure 4. The fiducial Earth profiles for each molecule are displayed in Figure 3. The last two rows show the mean percentage error (MPE) and characteristic vertical uncertainty (z_{err}) for each spectral fit.

Table 9. Retrieved parameters for Earth’s atmosphere from a fit to Earth’s high-resolution transmission spectrum in the 5 – 7.2 μm wavelength range using an evenly mixed atmospheric model (Model 2)

Parameters	Isothermal TP	avg	lat=0°	lat=19°	lat=41°	lat=66°	cold
T_0 [K]	203.02 ± 0.30	—	—	—	—	—	—
H ₂ O	−4.728 ± 0.012	−5.1029 ± 0.0040	−5.1714 ± 0.0041	−5.1685 ± 0.0041	−5.1606 ± 0.0048	−5.0899 ± 0.0040	−5.0496 ± 0.0039
CO ₂	−4.250 ± 0.039	−3.412 ± 0.010	−3.4084 ± 0.0098	−3.4080 ± 0.0099	−8.7712 ± 0.0072	−3.400 ± 0.011	−3.400 ± 0.011
O ₃	−5.735 ± 0.063	−5.872 ± 0.046	−5.867 ± 0.043	−5.867 ± 0.043	−4.917 ± 0.016	−5.863 ± 0.047	−5.864 ± 0.048
N ₂ O	−6.5775 ± 0.0026	−6.5565 ± 0.0020	−6.4875 ± 0.0019	−6.4798 ± 0.0019	−6.6952 ± 0.0036	−6.1504 ± 0.0019	−6.1677 ± 0.0019
CO	−6.6568 ± 0.0085	−6.7459 ± 0.0066	−6.7078 ± 0.0064	−6.7070 ± 0.0065	−6.823 ± 0.011	−6.6712 ± 0.0068	−6.6794 ± 0.0069
CH ₄	−5.502 ± 0.075	−5.794 ± 0.064	−5.795 ± 0.061	−5.795 ± 0.061	−4.663 ± 0.021	−5.795 ± 0.064	−5.794 ± 0.066
O ₂	−0.380 ± 0.047	−0.724 ± 0.073	−0.767 ± 0.071	−0.760 ± 0.046	−2.51 ± 0.22	−0.733 ± 0.069	−0.723 ± 0.077
N ₂	−0.47 ± 0.13	−0.15 ± 0.10	−0.18 ± 0.10	−0.179 ± 0.066	−2 ± 11	−0.159 ± 0.095	−0.15 ± 0.11
HNO ₃	−8.4615 ± 0.0024	−8.4700 ± 0.0017	−8.4733 ± 0.0017	−8.4671 ± 0.0017	−8.7898 ± 0.0026	−8.3149 ± 0.0017	−8.2996 ± 0.0017
NO ₂	−9.1052 ± 0.0034	−8.7527 ± 0.0023	−8.8008 ± 0.0023	−8.7969 ± 0.0023	−9.1356 ± 0.0028	−8.7967 ± 0.0024	−8.7754 ± 0.0024
MPE	14.38%	14.68%	14.60%	14.66%	17.04%	14.54%	14.42%
z_{err}	2.60 km	2.40 km	2.40 km	2.42 km	3.49 km	2.43 km	2.41 km

NOTE—CFC-11 and CFC-12 were not constrained and are therefore omitted from the table. Columns with fixed TP profiles are labeled in reference to those shown in Figure 4. The expected Earth profiles for each molecule are displayed in Figure 3, with the approximate \log_{10} VMRs for Earth’s atmosphere given in Table 1. The last two rows show the mean percentage error (MPE) and characteristic vertical uncertainty (z_{err}) for each spectral fit.

the transit depth as,

$$\Delta F = \left(\frac{R_p + z_{eff}(\lambda)}{R_s} \right)^2 \quad (3)$$

where R_p is TRAPPIST-1e’s assumed solid body surface radius (0.915 R_\oplus ; Grimm et al. 2018), $z_{eff}(\lambda)$ is the wavelength-dependent effective transit altitude from M&C19, and R_s is the TRAPPIST-1 stellar radius (0.121 R_\odot ; Van Grootel et al. 2018).

We used the PANDEXO noise model (version 2.0; Batalha et al. 2017b; Batalha et al. 2018) to gener-

ate synthetic JWST observations of our TRAPPIST-1e Earth model with both the NIRSpec G395M (Bagnasco et al. 2007; Ferruit et al. 2014) and MIRI LRS (Bouchet et al. 2015; Kendrew et al. 2015) instruments. These two instruments were selected for this analysis because they span different, yet contiguous, spectral regions from one another, they fully overlap with the observed wavelength range of the M&C19 spectrum, and they are ideal instruments for terrestrial exoplanet transmission spectroscopy (Lustig-Yaeger et al. 2019). Although NIRSpec PRISM is also an optimal JWST instrument mode to

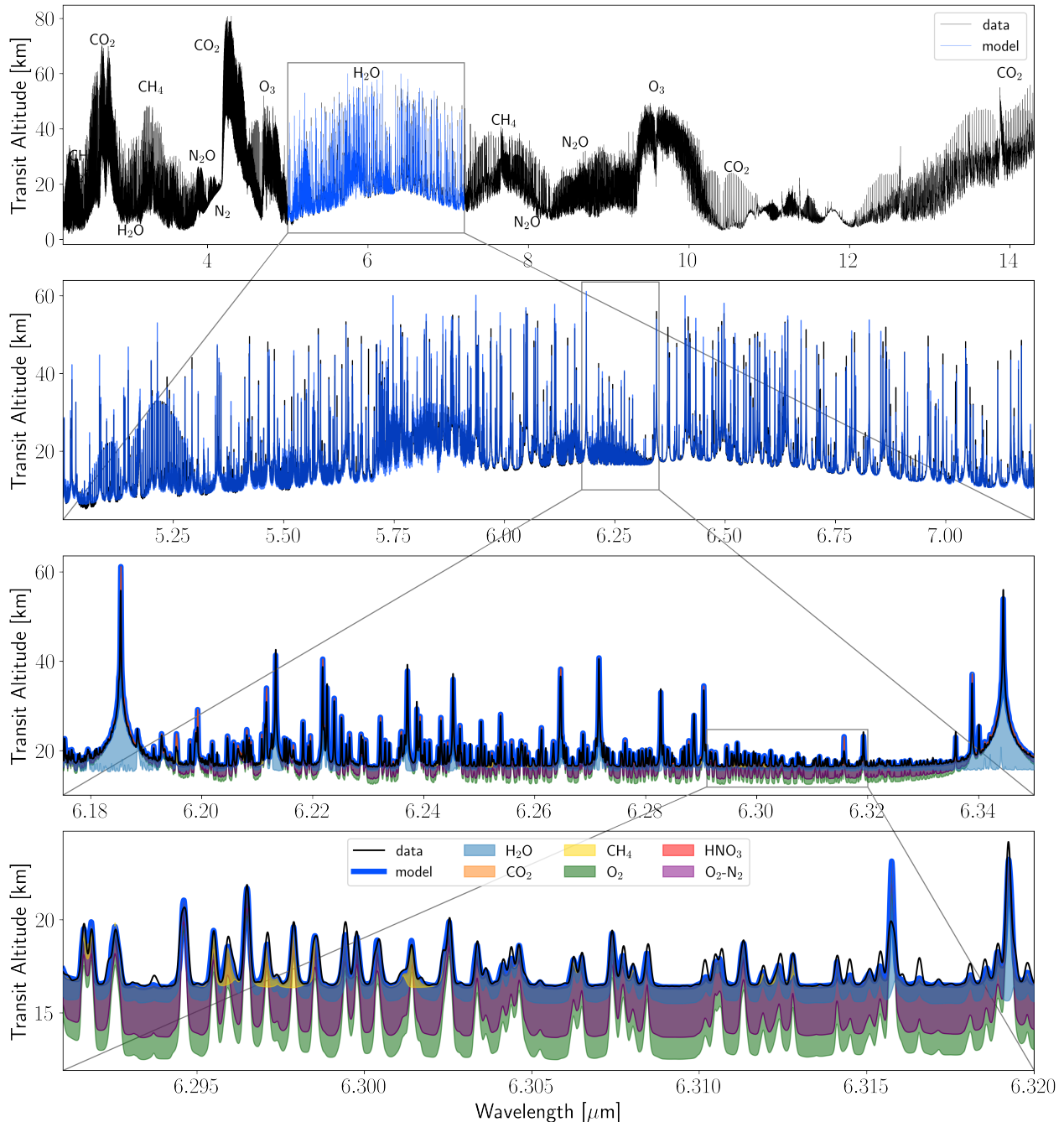


Figure 10. Best fit model of Earth’s high resolution transmission spectrum in the 5 – 7.2 μm wavelength range using the 66° latitude TP profile. The data are shown in black, the best-fitting model spectrum is shown in blue, and various colors are used in the bottom panels to indicate each molecule’s contribution to the model spectrum. The shading for O_2 indicates the contribution from both $\text{O}_2\text{--O}_2$ CIA and $\text{O}_2\text{--N}_2$ CIA. In the bottom panel, HNO_3 , CH_4 , and H_2O show subtle absorption features above a $\text{O}_2\text{--N}_2$ CIA, $\text{O}_2\text{--O}_2$ CIA, and H_2O continuum.

use for TRAPPIST-1 observations, the shortwave cutoff for PRISM is $0.6 \mu\text{m}$ and the M&C19 spectrum only extends down to $2.2 \mu\text{m}$. As a result, we focus primarily on the NIRSPEC G395M mode, which spans $2.87\text{--}5.10 \mu\text{m}$, but we show and discuss a selected PRISM simulation in Appendix B for data from $2.2\text{--}5.2 \mu\text{m}$. We simulate

noise on each observation for 80 stacked transits, which is approximately the maximum number of observable transits of TRAPPIST-1e in the nominal 5-year JWST mission lifetime. This allows us to compare the atmospheric constraints retrieved from each instrument using a uniform amount of telescope time.

For our TRAPPIST-1e retrievals, we make a few adjustments to our model to better compare with standard exoplanet methodologies. First, we only fit for the following molecules: H_2O , CO_2 , CH_4 , O_2 , O_3 , and CO . We use “Model 2” for this investigation, which assumes that these gases are evenly mixed throughout the atmospheric column and fits for their log volume mixing ratios and the isothermal temperature. Second, we also include as free parameters the solid body surface radius with uniform prior $\mathcal{U}(0.865, 0.965) R_\oplus$ and the log-surface pressure with uniform prior $\mathcal{U}(3, 6)$ Pa. Finally, we assume N_2 as the background gas in the atmosphere (e.g. Barstow et al. 2016; Krissansen-Totton et al. 2018; Changeat et al. 2019; Barstow et al. 2020), and now self-consistently determine the atmospheric mean molecular weight using the molecular composition of the forward model at each step in the retrieval.

Figure 11 compares our NIRSpec G395M (blue) and MIRI LRS (orange) transmission spectrum retrieval results for TRAPPIST-1e. The top row of subplots show 1D marginalized posterior distributions for the inferred atmospheric parameters. The histograms are compared to their spatially averaged vertical profiles in Earth’s atmosphere, which are shown in black as a function of pressure. The bottom two panels show our median fits to the synthetic JWST spectra with 1 and 3σ bounding envelopes. Although we binned the NIRSpec G395M data to a resolving power of $R = 150$ and the MIRI LRS data to $R = 50$ for visualization purposes, the spectra were fit at the native spectral resolution of each instrument ($R \sim 1000$ for NIRSpec G395M and $R \sim 100$ for MIRI LRS). Figure 13 in Appendix B provides the full corner plot with retrieved median and 1σ confidence intervals for each parameter and parameter covariances.

Given the same telescope time, JWST’s NIRSpec G395M instrument acquires higher S/N and higher resolution spectra than MIRI LRS, and the retrieved constraints on Earth’s atmosphere reflect these gains for NIRSpec. Using NIRSpec data we inferred (near) Gaussian posteriors for the abundances of CO_2 and CH_4 , peaked posteriors for O_3 but without a lower limit, and a credible upper limit for H_2O and CO . Each of these constraints is consistent with the true values in Earth’s atmosphere. In comparison, using MIRI LRS data we achieved relatively imprecise constraints on all gases. Only O_3 was accurately constrained to within three orders of magnitude with MIRI LRS (± 2.4 dex). Despite the presence of the strong $9.6 \mu\text{m}$ O_3 band falling within the MIRI LRS wavelength range, the presence of the $4.7 \mu\text{m}$ O_3 band within the NIRSpec G395M wavelength range enables NIRSpec to constrain O_3 about twice as precisely (± 0.91 dex). Neither instrument is able to con-

strain O_2 due to the lack of detectable bands in the 2–14 μm range, with the exception of broad CIA bands, which are well below the noise levels in the spectrum. Similarly, MIRI cannot place an upper limit on CO due to a lack of absorption features in the wavelength range. The MIRI CO_2 result has a misleading spike at high abundances due to the random white noise added to the synthetic data. This spike is eliminated in tests that omitted the randomized noise (see Appendix B). Unlike our previous retrievals of Earth’s transmission spectrum without noise, at JWST’s precision the complexity of retrieved atmospheric constraints are severely limited such that homogeneous vertical profiles are sufficient to capture the general characteristics of the atmosphere.

4. DISCUSSION

We analyzed the exoplanet-analog transmission spectrum of Earth from Macdonald & Cowan (2019) to perform a validation of our new exoplanet retrieval model, SMARTER, on the only known habitable and inhabited planet and to determine the capacity for transmission spectroscopy to retrieve signs of habitability and biosignatures. In general, we obtained excellent model fits to the high S/N observed spectra both in low resolution (Figure 5) and in high resolution (Figures 7, 9, 10) that demonstrate the validity of our model down to an equivalent precision of < 5 ppm for the exoplanet TRAPPIST-1e. We retrieved gas abundance estimates that are accurate within $\sim 25\%$ or better of the Earth average VMRs for the majority of the 12 molecules included in our study and demonstrated the limits to which a single set of 1D atmospheric profiles can be used to describe a dynamic 3D planet such as Earth. These results provide a detailed perspective on the global atmospheric environment that yields strong evidence of the planet’s habitability, presence of biosignatures, and technosignatures as seen through the lens of an exoplanet-analog transmission spectrum. Our analyses using errors consistent with JWST observations of the TRAPPIST-1 system (Figures 11 and 13) reveal a simpler picture of the atmosphere wherein a large time investment is required to constrain CH_4 and CO_2 to better than ± 1 dex and potentially provide a weak detection of O_3 , thereby illuminating practical challenges to characterizing transiting Earth-like exoplanets for habitability and biosignatures in the near term. We further elaborate on our model validation/limitations and the characterization of habitability and biosignatures in the following discussion.

4.1. Model Validation & Limitations

Our retrieved molecular abundances from the low resolution spectrum (Table 2) are consistent with the

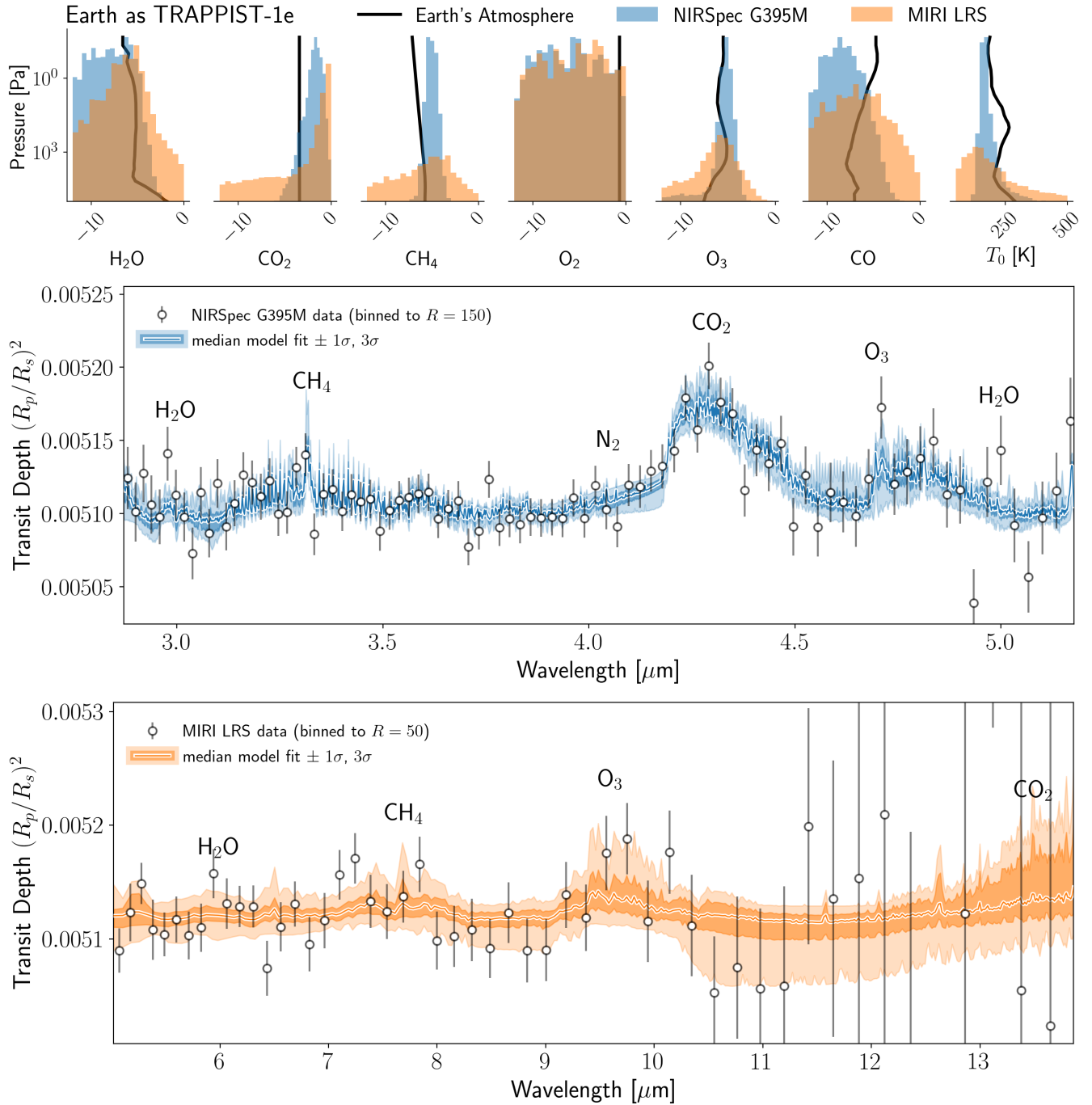


Figure 11. Fits to synthetic JWST spectra and the corresponding retrieved atmospheric constraints. The upper subplots show 1D marginalized posterior distributions for retrievals using NIRSpec G395M data (blue) and MIRI LRS data (orange) compared to the true vertical profiles exhibited by Earth’s atmosphere (black lines). The middle and bottom panels show the synthetic JWST spectra for 80 stacked transits of TRAPPIST-1e observed with NIRSpec G395M and MIRI LRS, respectively, along with the $\pm 1\sigma$ and 3σ uncertainty envelopes around the median model fits.

Earth’s atmospheric composition within the range of spatial and temporal variability exhibited across the globe (Table 3). Specifically, in the noiseless data, we retrieved volume mixing ratios for H₂O, CO₂, O₃, N₂O, CH₄, and N₂ that are within 28% of their average Earth

values. Using TP profiles and mixing ratio profiles that vary with altitude provided better fits to the Earth spectrum (5% errors) that yield more accurate abundance constraints than 1D isothermal TP structures with evenly-mixed gas VMRs, although vertically homo-

geneous 1D atmospheric models still provided a good fit to the data (12% errors) that enabled a relatively accurate assessment of the atmospheric composition (see Table 2 and Figure 6), considering the simplicity of the model.

Our retrievals using evenly mixed molecular profiles provided $2.6\times$ worse fits to the observations on average than retrievals that scaled the characteristic vertical profiles of each gas. This remained consistent in both low resolution and high resolution. Thus information about the vertical distribution of gases exists in pristine transmission spectrum measurements that can in theory be used to retrieve vertically resolved molecular profiles, consistent with the modeling results of [Changeat et al. \(2019\)](#). The improvements seen for the model with realistic vertical structure, however, were at the level of <5 ppm equivalent precision for observations of TRAPPIST-1e and therefore insignificant for near term studies of rocky exoplanets. While our evenly mixed retrieval on the case with 10% noise added (Figure 6) also indicated vertical sensitivity in the $9.6\ \mu\text{m}$ O_3 band, our retrievals using JWST analog data further indicated that evenly mixed atmospheric models with isothermal TP profiles will suffice to accurately interpret terrestrial exoplanet transmission spectra with JWST.

We investigated multiple different characteristic Earth TP profiles (Figure 4) for retrievals of the high resolution spectrum and found that each one provided a slightly different fit to the high-res data that yielded accurate retrievals for different gases (Table 8). Statistically significant differences in the retrieved gas abundances were found using different characteristic TP profiles. While a low latitude TP profile provided the most accurate retrieval of the CO_2 abundance, N_2 and O_2 were most accurately retrieved using a colder TP profile representative of higher latitudes. These results indicate that such high resolution transmission spectra are sensitive to atmospheric thermal structure, but likewise illuminates a degeneracy between the TP structure and the gas abundances. These complicating factors warrant investigation in future works aimed at retrieving a characteristic altitude-dependent TP profile for Earth. However, it is possible that even such an approach may still impose biases in gas abundances because the globally-averaged exoplanet-analog transmission spectrum from [Macdonald & Cowan \(2019\)](#) contain information from more than one characteristic TP profile. These results for Earth echo the findings obtained from modeling giant exoplanet atmospheres, such as [Caldas et al. \(2019\)](#) (see also, [Lacy & Burrows 2020](#); [Pluriel et al. 2020](#); [Wardenier et al. 2022](#)) where GCM outputs were used to produce a 3D exoplanet transmission spectrum, which

could be well-fit with a simple 1D atmospheric retrieval model, but doing so caused biases in gas abundances that could be challenging to diagnose in real data. Thus, even though each choice of TP profile that we used provided an excellent fit to the data, in reality none of them are correct because the data provides a sampling of all TP profiles along the terminator—an intrinsically 3D effect.

Our retrievals of Earth’s high resolution transmission spectrum near $6\ \mu\text{m}$ revealed challenges associated with fitting the spectral continuum that, if addressed, could potentially be leveraged for more precise exoplanet atmospheric characterization. Resolving the spectral continuum between H_2O (and other gas) lines enabled the abundances of O_2 and N_2 to be retrieved due to the presence of broad $\text{O}_2\text{--O}_2$ and $\text{O}_2\text{--N}_2$ CIA bands (Figure 10) near $6\ \mu\text{m}$ (see also, [Fauchez et al. 2020](#)). However, the accuracy of this approach depended on the specific choice of TP and H_2O vertical profiles. In an exoplanet context, this assumption would not be appropriate *a priori* and would therefore open up a complicated degeneracy between the TP profile, and the VMRs of H_2O , O_2 , and N_2 . We also note that these $6\ \mu\text{m}$ CIA bands were not accessible in the low resolution spectrum due to the convolution of the strong H_2O lines with the spectral continuum.

Furthermore, the challenges and opportunities afforded to high resolution spectroscopy may be best realized for exoplanets with the upcoming generation of ground-based extremely large telescopes (ELTs; [Johns et al. 2012](#); [Skidmore et al. 2015](#); [Marconi et al. 2016](#)). These telescopes rely on high resolution spectroscopy to distinguish exoplanet atmospheric features from telluric lines (e.g., [Snellen et al. 2013](#); [Brogi & Line 2019](#); [Hood et al. 2020](#); [Leung et al. 2020](#); [Currie et al. 2023](#)), and are therefore well suited to investigate, and may need to properly account for, the confounding TP profile and line/continuum effects discussed here. Moreover, our validated model SMARTER is an excellent tool for generating forward models and performing retrieval simulations at high spectral resolution. Future work using the high-resolution cross-correlation likelihood formulation of [Brogi & Line \(2019\)](#) will aim to assist ground-breaking ELT science cases. However, high-resolution ground-based observations longward of $5\ \mu\text{m}$ may be prohibitively challenging due to thermal background noise. As such, our high-resolution findings in the MIR may not be observable in the near term, but rather, may serve as potential motivation for a mission concept or technique that is capable of overcoming the thermal background, likely from space.

The fact that the empirical transmission spectrum from M&C19 omitted occultation measurements with clouds has likely impacted our retrieval results and limits the scope of our study to clear sky phenomena. Since the M&C19 transmission spectrum represents the spatially and temporally averaged Earth *only along clear optical paths through the atmosphere*, this spectrum naturally contains an intrinsic bias towards atmospheric characteristics that correlate with clear skies. This could potentially explain deviations found between our retrieved atmospheric characteristics and known average values, but other factors—such as the latitudinal, seasonal, and temporal sampling of the SCISAT ACE-FTS data—cannot be ruled out. Furthermore, our results associated with the transmission spectrum continuum, including sensitivity to CIA features (Figure 10) and refraction effects (Figure 12), will be further complicated for exoplanets where clear skies cannot be assumed. Optically thick clouds (and/or hazes) are well known to truncate the path length of light, particularly in the transit geometry (Fortney 2005), and have been responsible for the flat and featureless transmission spectra of numerous gaseous exoplanets (e.g., Kreidberg et al. 2014; Knutson et al. 2014), and are also a candidate for the flat JWST transmission spectrum of a rocky exoplanet (Lustig-Yaeger & Fu et al. 2023). In particular, partially cloudy Earth-like exoplanets will exhibit a confounding combination of clear and cloudy effects, where broad CIA bands, refraction, and clouds may all appear degenerate in retrieval analyses. Further exoplanet-analog observations and analyses of Earth and other Solar System planets in transit would be beneficial for disentangling these complicated processes (e.g., Mayorga et al. 2021). The recent work of Doshi et al. (2022) suggests that Earth’s clouds are sufficiently low-altitude as to not appreciably impact transmission observations of Earth-like exoplanets transiting M dwarfs, however 3D GCM models with full atmospheric dynamics do show an impact of higher altitude clouds in the transmission spectra of similar exoplanets (Komacek et al. 2020; May et al. 2021), so the general outcome for JWST observations remains uncertain and requires both data and modeling.

To further shed light on our findings in the context of upcoming exoplanet observations, we analyzed Earth’s spectrum using the spectral resolution and precision calculated for a long observational campaign of TRAPPIST-1e with JWST. We found that NIR observations with NIRSpec significantly outperformed MIR observations with MIRI LRS for obtaining atmospheric constraints given equal observing times with each instrument. These results are in agreement with other studies

that have compared JWST instruments for rocky exoplanet transmission spectroscopy (Lustig-Yaeger et al. 2019; Fauchez et al. 2019; Pidhorodetska et al. 2020). We retrieved an abundance constraint for O₃ that was approximately 2 orders of magnitude more precise using the 4.7 μm O₃ band with NIRSpec G395 compared to the much more prominent 9.6 μm O₃ band with MIRI LRS, and conclude that, given current detector and telescope capabilities, O₃ may be best sought at shorter NIR wavelengths rather than in the MIR. This result is consistent with the findings of Krissansen-Totton et al. (2018) and highlights the importance of considering wavelength-dependent instrument sensitivity, and not just molecular absorption band strength, when targeting specific molecules. However, we caution that by using the true Earth transmission spectrum in our TRAPPIST-1 JWST assessment, atmospheric photochemistry for this M dwarf planet has not been considered. Photochemistry can modify the vertical O₃ structure (e.g. Segura et al. 2005; Rugheimer et al. 2015; Kaltenecker & Lin 2021; Meadows et al. 2018b) and is expected to enhance the CH₄ detectability, and reduce the stratospheric abundance and detectability of O₃ for TRAPPIST-1e relative to the modern Earth atmosphere with solar UV forcing (Meadows et al. 2023).

Our simplified atmospheric model with an isothermal and evenly mixed vertical structure provided good fits to the synthetic JWST spectra that were consistent with the true Earth values within the inferred uncertainties. Given the optimistic nature of our synthetic JWST observations—80 stacked transits of TRAPPIST-1e—we suggest that this common assumption may be sufficient for terrestrial exoplanet retrieval modeling in the JWST era, although more work is warranted in this area to avoid the inference biases that we identified in the high S/N Earth spectra and that have been reported in the literature for gaseous exoplanets retrieval modeling (e.g., Rocchetto et al. 2016; Caldas et al. 2019; MacDonald et al. 2020).

Thus far we have discussed how model simplifications and the 3D time-varying nature of Earth’s atmosphere may explain deviations between our findings and the true Earth spectrum and atmosphere. However, systematic effects from the ACE-FTS instrument may also play a confounding role in these deviations. In particular, the lack of temperature coherence likely produced systematic errors on the order of a few percent in the Earth averaged spectrum (Boone & Bernath 2019). The metrology laser for the ACE-FTS instrument does not have a fixed wavelength because it changes with ambient temperature. This can lead to small shifts in wavenumber, and as a result, lines in the average spectra will ex-

perience a slight artificial broadening. In an individual occultation, the relative intensities of different lines in the spectrum are well characterized using a single (ambient) temperature. In the average spectrum, the relative intensities of different lines are not perfectly characterized by a single value of temperature, and likely results in systematic errors the order of a few percent.

Owing primarily to its line-by-line approach, the computational expense of SMARTER exceeds the typical run time of other current exoplanet atmospheric retrieval models, which in turn limits how and when it may be optimally used. The time required to evaluate the SMARTER forward model is driven primarily by the breadth of the wavelength range, since SMART operates with a high internal wavenumber resolution that is set by the density of molecular lines in the wavelength range, regardless of the resolution of the data. For example, the full 2 – 14 μm spectral models in Section 3.1 required approximately 2 minutes per likelihood evaluation (on a cluster processor), while the narrower 4 μm simulations required approximately 30 seconds per evaluation. The aforementioned approach of resampling the molecular absorption coefficients speeds up the forward model considerably, while incurring modeling errors at or below 1%. Using this approach the 2 – 14 μm spectrum ran in about 15 seconds, and each JWST instrument in 2-6 seconds. Since the retrieval iterates over successive calls to the forward model, computationally expensive forward models cascade into very slow retrievals. Our OE retrievals required fewer than 1000 evaluations on average to reach convergence, whereas our DYNASTY retrievals required approximately 100,000 forward model evaluations. Although SMARTER can be used generally to retrieve atmospheres from the transmission, emission, and reflected-light spectra of a diversity of planet types, given the computational considerations, we see SMARTER as a uniquely robust, specialized model that may be optimally used on specific high priority simulated or observed targets to (1) explore the effects of physical rigor and radiative transfer complexity in exoplanet retrievals, (2) fit high resolution spectra, and (3) analyze targets where the results from SMARTER are well worth the computational expense. However, science cases involving numerous retrievals or large parameter sweeps are not ideal for SMARTER and should use other capable, faster retrieval models (e.g., see MacDonald & Batalha 2023, and references therein).

4.2. Detecting Habitability & Biosignatures using Transmission Spectroscopy

Assessing the habitability of an exoplanet and confirming the presence of biosignatures will be a challeng-

ing endeavor for upcoming exoplanet observations, requiring the detection of specific spectroscopic indicators (Schwieterman et al. 2018; Robinson 2017b) synthesized together with contextual clues into the nature of the planetary environment in which these indicators reside (Meadows et al. 2018a; Meadows & Barnes 2018). While we found that the broad wavelength, impeccably high S/N observation that we analyzed contained many these essential ingredients, transmission spectroscopy is limited in terms of information that can be gleaned about the planetary surface environment, which then limits the strength of habitability and biosignature conclusions.

Through the eyes of JWST quality measurements, assessing the habitability and inhabited nature of Earth is challenging and leaves much unknown about the atmosphere. Although we obtained compelling abundance constraints for CH_4 , CO_2 , O_3 , and H_2O using simulated NIRSpec observations for an exhaustive 80 transit campaign of TRAPPIST-1e, the habitability of the planet is not readily apparent in our findings. Our retrieved H_2O abundance is not consistent with that at the Earth’s surface, but instead it is most consistent with the upper troposphere. Similarly, the characteristic isothermal TP profile that we retrieved is most consistent with the upper atmosphere. Thus, the insensitivity of the transmission spectrum to the surface limits habitability assessments even using relatively high quality observations with JWST. The simultaneous presence of CO_2 , CH_4 , and O_3 are indeed a biosignature that JWST could potentially detect for an Earth-like planet, but may prove challenging to interpret without contextual knowledge about the habitable environment.

Our inferences about Earth’s atmosphere from the *noiseless* exoplanet-analog transmission spectrum provide compelling evidence in support of the planet’s habitable surface conditions and presence of a global biosphere that has and continues to significantly modify the atmospheric composition. We will now walk through the lines of evidence that can be used to support this claim by considering the bulk atmospheric composition, the atmospheric indicators of habitability, and the detection of specific biosignature and technosignature gases.

Evidence of Earth’s primarily N_2 and O_2 bulk atmospheric composition proved to be one of the most subtle and difficult signals to interpret from the transmission spectrum observations. We were able to roughly infer the volume mixing ratio of N_2 ($\sim 80\%$), particularly in high resolution spectra, and thereby identify N_2 as the bulk atmospheric constituent. This finding depended almost exclusively on the 4.1 μm N_2 – N_2 CIA feature that resides in the wings of the 4.3 μm CO_2 band (see Figure 5). This underscores the previous findings of Schwi-

eterman et al. (2015b) by demonstrating that exoplanet transmission spectroscopy observations can target this N_2 CIA band in the future as a means to detect and constrain the abundance of N_2 in terrestrial atmospheres. This also agrees with similar findings for N_2-N_2 CIA that were obtained by Kaltenegger et al. (2020) in the context of an Earth-like planet transiting a white dwarf, where high S/N transmission spectra may be more readily achieved. At MIR wavelengths near $6 \mu\text{m}$, the spectral continuum appears to be dominated by partial contributions from N_2-O_2 CIA, O_2-O_2 CIA, and H_2O line absorption wings (see Figure 10). These three absorbing species were degenerate in our model fits and proved difficult to accurately constrain without imposing a specific choice of TP profile. Constraining the atmospheric mean molecular weight can provide another line of evidence for the bulk atmospheric composition, however we did not vary it in our retrievals.

We were able to infer the presence and abundance of H_2O vapor in Earth’s atmosphere from a combination of absorption features in the near- and mid-IR. Our VMR constraints are consistent with upper tropospheric water abundances, which supports the interpretation of Earth as a habitable planet. Crucially, the small and subtle nature of water features in Earth’s transmission spectrum—while difficult to remotely sense—is a good sign for habitability because substantial water features would indicate abundant stratospheric water vapor, which may indicate that the planet is in a runaway greenhouse state and is therefore uninhabitable (Goldblatt & Watson 2012). Furthermore, our assessment of atmospheric CO_2 provides important contextual clues into the climatic state of the planet that would greatly aid in the indirect assessment of habitability. However, assessing exoplanet habitability from transmission spectroscopy alone may not provide sufficient evidence due to difficulty sensing the surface, including surface temperature and pressure estimates, the near-surface H_2O abundance, and abundances of other greenhouse gases. In the absence of more direct methods for habitability assessment (e.g. Cowan et al. 2009; Robinson et al. 2010; Lustig-Yaeger et al. 2018), these quantities would all be required for climate models to accurately simulate the likelihood of unobserved liquid water existing on the planetary surface (Meadows & Barnes 2018). Our high resolution investigations yielded sensitivity to the vertical thermal structure and H_2O profile, which could be used to detect the atmospheric cold trap that keeps water vapor concentrated in Earth’s lower atmosphere. Since we found that retrievals using realistic vertical structure provided better fits to the spectra than assuming even mixing, future studies should further in-

vestigate the potential for vertically resolved water vapor retrievals to enhance the robustness of indirect exoplanet habitability assessments.

We retrieved robust constraints on the presence and abundance of numerous classical biosignature gases and disequilibrium biosignature pairs. In particular, we retrieved robust constraints on O_3 from the prominent $4.7 \mu\text{m}$ and $9.65 \mu\text{m}$ absorption bands. O_3 forms from the photolysis of photosynthetically produced O_2 , which we were notably not able to detect due to O_2 lacking prominent absorption features in the $2 - 14 \mu\text{m}$ wavelength range. O_3 has been proposed as a proxy for O_2 for MIR exoplanet observations (Léger et al. 1993, 2011; Des Marais et al. 2002), which is strongly supported by our analyses of O_2 and O_3 in the observed transmission spectrum. We retrieved the CH_4 abundance from the 2.3 , 3.3 , and $7.7 \mu\text{m}$ absorption bands, which exists in Earth’s atmosphere as a result of geological sources (Etiope & Sherwood Lollar 2013), methanogenesis from anaerobic single-celled microbes, and anthropogenic sources (Schwieterman et al. 2018). The simultaneous presence of CH_4 alongside O_3 is a compelling biosignature pair because CH_4 is thermodynamically disfavored in an oxidized atmosphere and must therefore originate from a strong flux source. We also retrieved the abundance of N_2O , which is a biogenic product of incomplete denitrification of NO_3^- to N_2 gas and has minimal abiotic sources (Schwieterman et al. 2018). N_2O has been proposed as a strong biosignature (Segura et al. 2005; Rugheimer et al. 2015). Our sensitivity to N_2O derives primarily from features at 4.5 , 7.8 , and $8.6 \mu\text{m}$. We also detected and retrieved the abundance of NO_2 primarily using the absorption feature at $6.2 \mu\text{m}$. NO_2 was recently proposed as a possible technosignature due to its anthropogenic production from combustion processes (Kopparapu et al. 2021). Finally, we constrained the abundance of the chlorofluorocarbons (CFCs) CFC-11 and CFC-12 at 11.8 and $10.8 \mu\text{m}$, respectively. CFCs have also been proposed as technosignatures due to their many industrial applications and infamy catalyzing the destruction of O_3 (Marinova et al. 2005; Schneider et al. 2010; Lin et al. 2014; Haqq-Misra et al. 2020).

Taken together, these climate and habitability indicators (e.g., H_2O , CO_2 , CO), biosignatures (e.g., O_3 , CH_4 , N_2O , O_2), and technosignatures (e.g., NO_2 , CFC-11, CFC-12) paint a striking picture of the modern Earth as a living planet. However, despite the robust detection of individual touchstone molecules and their respective abundances in the noiseless M&C19 data, the claim that we have detected life, while perhaps evident, remains unquantified. Likewise, the confidence of life de-

tection from our results using simulated exoplanet observations with JWST, while surely much lower, is not readily quantified. Such gaps in the statistical astrobiology used for life detection have recently been illuminated as requiring significant focus and broad interdisciplinary engagement (e.g., Catling et al. 2018; Green et al. 2021; Meadows & Graham 2022). The data analyses undertaken here as well as the empirical Earth spectrum from M&C19 may serve as an important resource to test and validate life detection frameworks as they are put forth.

5. CONCLUSION

In this paper, we validated our terrestrial exoplanet atmospheric retrieval model SMARTER against a high resolution, high S/N empirical transmission spectrum of Earth and were able to retrieve abundances for the majority of spectrally active molecules to better than 25% while maintaining residuals below 5 ppm equivalent precision for TRAPPIST-1 observations. The presence and abundance of retrieved gases provides compelling evidence of the planet’s habitable surface conditions, global biosphere, and emerging technosphere as viewed exclusively through the analysis of an exoplanet-analog transmission spectrum. Although the data wavelength range did not contain ro-vibrational or electronic transitions for the Earth’s bulk atmospheric gases, N₂ and O₂, nonetheless we were able to roughly constrain their abundances using collisionally-induced absorption features at high spectral resolution where they could be distinguished from overlying absorption lines.

When we degraded the empirical spectrum down to the spectral resolution and precision of expected JWST/NIRSpec observations, even after coadding all of the transits available in the nominal 5-year mission, we were only able to obtain robust abundance constraints for CO₂ and CH₄, with a tentative indication of O₃.

Just as observations and retrievals of extrasolar giant planets are leading the way towards future analyses of Earth-like exoplanets with higher-sensitivity instruments, the study of Earth provides high-precision exoplanet-analog data that can prepare our exoplanet models to interpret vertically complex and spatially dy-

namic 3D atmospheres, beginning with near-term studies of extrasolar giant planets. The Earth transmission spectrum from M&C19 is a treasure trove of information on the physics and chemistry of exoplanet transmission spectroscopy in the limit of high precision and resolution. In this work we have only begun to scratch the surface of what is possible with this benchmark dataset, and we encourage community engagement with these data for continued model validations and upgrades as the field progresses towards the precise characterization of Earth-like exoplanets.

We would like to sincerely thank E. Macdonald for providing the spectrum that made our investigation possible, as well as N. Cowan and C. Boone for useful discussions. We also thank two anonymous reviewers for their thorough reviews of our manuscript and thoughtful comments that helped to improve the quality, clarity, and reproducibility of our work. This work was performed by the Virtual Planetary Laboratory Team, which is a member of the NASA Nexus for Exoplanet System Science, and funded via NASA Astrobiology Program Grant 80NSSC18K0829. J.L.Y acknowledges support from JHU APL’s Independent Research And Development program. This work made use of the advanced computational, storage, and networking infrastructure provided by the Hyak supercomputer system at the University of Washington. Some of the results in this paper were derived using the healpy and HEALPix package.

Software: Astropy (Astropy Collaboration et al. 2013; Price-Whelan et al. 2018), Dynesty (Speagle 2020), HEALPix (Górski et al. 2005), healpy (Zonca et al. 2019), LBLABC (Meadows & Crisp 1996), Matplotlib (Hunter 2007), MultiNest (Feroz & Hobson 2008; Feroz et al. 2009), NumPy (van der Walt et al. 2011; Harris et al. 2020), SciPy (Virtanen et al. 2019; Virtanen et al. 2020), SMART (Meadows & Crisp 1996), SMARTER (this paper; Lustig-Yaeger et al. 2022), Pandas (Pandas Development Team 2020), Pandeia (Pontoppidan et al. 2016), PandExo (Batalha et al. 2017b; Batalha et al. 2018), pysynphot (STScI Development Team 2013)

REFERENCES

- Aizawa, M., Kawahara, H., & Fan, S. 2020, ApJ, 896, 22
- Arney, G., Meadows, V., Crisp, D., et al. 2014, Journal of Geophysical Research (Planets), 119, 1860
- Arney, G., Domagal-Goldman, S. D., Meadows, V. S., et al. 2016, Astrobiology, 16, 873
- Arney, G. N., Meadows, V. S., Domagal-Goldman, S. D., et al. 2017, ApJ, 836, 49
- Arnold, L., Ehrenreich, D., Vidal-Madjar, A., et al. 2014, A&A, 564, A58
- Astropy Collaboration, Robitaille, T. P., Tollerud, E. J., et al. 2013, A&A, 558, A33

- Bagnasco, G., Kolm, M., Ferruit, P., et al. 2007, in Proc. SPIE, Vol. 6692, Cryogenic Optical Systems and Instruments XII, 66920M
- Baranov, Y. I., Lafferty, W. J., & Fraser, G. T. 2004, Journal of Molecular Spectroscopy, 228, 432
- Barstow, J. K., Aigrain, S., Irwin, P. G. J., Kendrew, S., & Fletcher, L. N. 2016, Monthly Notices of the Royal Astronomical Society, 458, 2657
- Barstow, J. K., Changeat, Q., Garland, R., et al. 2020, MNRAS, 493, 4884
- Barstow, J. K., & Heng, K. 2020, arXiv e-prints, arXiv:2003.14311
- Barstow, J. K., & Irwin, P. G. J. 2016, Monthly Notices of the Royal Astronomical Society, 461, L92
- Batalha, N., Stevenson, K., Hill, M., et al. 2018, natashabatalha/PandExo: Starting PandExo Releases, doi:10.5281/zenodo.1256955
- Batalha, N. E., Kempton, E. M. R., & Mbarek, R. 2017a, ApJL, 836, L5
- Batalha, N. E., Lewis, N. K., Line, M. R., Valenti, J., & Stevenson, K. 2018, ApJL, 856, L34
- Batalha, N. E., Mandell, A., Pontoppidan, K., et al. 2017b, Publications of the Astronomical Society of the Pacific, 129, 064501
- Benneke, B., & Seager, S. 2013, ApJ, 778, 153
- Bernath, P. F. 2017, JQSRT, 186, 3
- Bernath, P. F., McElroy, C. T., Abrams, M. C., et al. 2005, Geophys. Res. Lett., 32, L15S01
- Bétrémieux, Y., & Kaltenegger, L. 2014, The Astrophysical Journal, 791, 7
- Boone, C. D., & Bernath, P. F. 2019, JQSRT, 230, 1
- Bouchet, P., García-Marín, M., Lagage, P.-O., et al. 2015, PASP, 127, 612
- Broggi, M., De Kok, R. J., Birkby, J. L., Schwarz, H., & Snellen, I. A. 2014, Astronomy and Astrophysics, 565, 1
- Broggi, M., & Line, M. R. 2019, The Astronomical Journal, 157, 114
- Buchner, J., Georgakakis, A., Nandra, K., et al. 2014, A&A, 564, A125
- Caldas, A., Leconte, J., Selsis, F., et al. 2019, A&A, 623, A161
- Catling, D. C., Krissansen-Totton, J., Kiang, N. Y., et al. 2018, Astrobiology, 18, 709
- Changeat, Q., Edwards, B., Waldmann, I. P., & Tinetti, G. 2019, ApJ, 886, 39
- Charbonneau, D., Brown, T. M., Noyes, R. W., & Gilliland, R. L. 2002, ApJ, 568, 377
- Charnay, B., Meadows, V., Misra, A., Leconte, J., & Arney, G. 2015, The Astrophysical Journal Letters, 813, L1
- Clough, S., Kneizys, F., & Davies, R. 1989, Atmospheric research, 23, 229
- Cowan, N. B., & Strait, T. E. 2013, ApJL, 765, L17
- Cowan, N. B., Agol, E., Meadows, V. S., et al. 2009, ApJ, 700, 915
- Crisp, D. 1997, Geophys. Res. Lett., 24, 571
- Crisp, D., Meadows, V. S., Bézard, B., et al. 1996, J. Geophys. Res., 101, 4577
- Cubillos, P., Blečić, J., Harrington, J., et al. 2016, BART: Bayesian Atmospheric Radiative Transfer fitting code, ascl:1608.004
- Currie, M. H., Meadows, V. S., & Rasmussen, K. C. 2023, PSJ, 4, 83
- Dalba, P. A., Muirhead, P. S., Fortney, J. J., et al. 2015, ApJ, 814, 154
- Damiano, M., & Hu, R. 2020, AJ, 159, 175
- Des Marais, D. J., Harwit, M. O., Jucks, K. W., et al. 2002, Astrobiology, 2, 153
- Doshi, D., Cowan, N. B., & Huang, Y. 2022, MNRAS, 515, 1982
- Dyudina, U., Zhang, X., Li, L., et al. 2016, ApJ, 822, 76
- Dyudina, U. A., Sackett, P. D., Bayliss, D. D. R., et al. 2005, ApJ, 618, 973
- Etiopie, G., & Sherwood Lollar, B. 2013, Reviews of Geophysics, 51, 276
- Fan, S., Li, C., Li, J.-Z., et al. 2019, ApJL, 882, L1
- Faucher, T. J., Turbet, M., Villanueva, G. L., et al. 2019, The Astrophysical Journal, 887, 194
- Faucher, T. J., Villanueva, G. L., Schwieterman, E. W., et al. 2020, Nature Astronomy, 4, 372
- Faucher, T. J., Villanueva, G. L., Sergeev, D. E., et al. 2022, PSJ, 3, 213
- Feng, Y. K., Line, M. R., Fortney, J. J., et al. 2016, ApJ, 829, 52
- Feng, Y. K., Robinson, T. D., Fortney, J. J., et al. 2018, AJ, 155, 200
- Feroz, F., Hobson, M., & Bridges, M. 2009, Monthly Notices of the Royal Astronomical Society, 398, 1601
- Feroz, F., Hobson, M., Cameron, E., & Pettitt, A. 2013, arXiv preprint arXiv:1306.2144
- Feroz, F., & Hobson, M. P. 2008, Monthly Notices of the Royal Astronomical Society, 384, 449
- Feroz, F., Hobson, M. P., Cameron, E., & Pettitt, A. N. 2019, The Open Journal of Astrophysics, 2, 10
- Ferruit, P., Birkmann, S., Böker, T., et al. 2014, in Proc. SPIE, Vol. 9143, Space Telescopes and Instrumentation 2014: Optical, Infrared, and Millimeter Wave, 91430A
- Foreman-Mackey, D., Hogg, D. W., Lang, D., & Goodman, J. 2013, PASP, 125, 306

- Fortney, J. J. 2005, *MNRAS*, 364, 649
- Foucher, P. Y., Chédin, A., Armante, R., et al. 2011, *Atmospheric Chemistry & Physics*, 11, 2455
- Fujii, Y., Kawahara, H., Suto, Y., et al. 2011, *ApJ*, 738, 184
- Fujii, Y., Lustig-Yaeger, J., & Cowan, N. B. 2017, *AJ*, 154, 189
- Fukabori, M., Nakazawa, T., & Tanaka, M. 1986, *Journal of Quantitative Spectroscopy and Radiative Transfer*, 36, 265
- García Muñoz, A., Zapatero Osorio, M. R., Barrena, R., et al. 2012, *ApJ*, 755, 103
- Gialluca, M. T., Robinson, T. D., Rugheimer, S., & Wunderlich, F. 2021, *PASP*, 133, 054401
- Gillon, M., Jehin, E., Lederer, S. M., et al. 2016, *Nature*, 533, 221
- Gillon, M., Triaud, A. H. M. J., Demory, B.-O., et al. 2017, *Nature*, 542, 456
- Goldblatt, C., & Watson, A. J. 2012, *Philosophical Transactions of the Royal Society of London Series A*, 370, 4197
- Gordon, I. E., Rothman, L. S., Hill, C., et al. 2017, *JQSRT*, 203, 3
- Górski, K. M., Hivon, E., Banday, A. J., et al. 2005, *ApJ*, 622, 759
- Green, J., Hoehler, T., Neveu, M., et al. 2021, *Nature*, 598, 575
- Greenblatt, G. D., Orlando, J. J., Burkholder, J. B., & Ravishankara, A. R. 1990, *J. Geophys. Res.*, 95, 18,577
- Greene, T. P., Line, M. R., Montero, C., et al. 2016, *The Astrophysical Journal*, 817, 17
- Grimm, S. L., Demory, B.-O., Gillon, M., et al. 2018, *A&A*, 613, A68
- Gruszka, M., & Borysow, A. 1997, *Icarus*, 129, 172
- Gu, L., Zeng, Z.-C., Fan, S., et al. 2022, *AJ*, 163, 285
- Gu, L., Fan, S., Li, J., et al. 2021, *AJ*, 161, 122
- Hanke, M., Umann, B., Uecker, J., Arnold, F., & Bunz, H. 2003, *Atmospheric Chemistry & Physics*, 3, 417
- Haqq-Misra, J., Kopparapu, R. K., & Schwieterman, E. 2020, *Astrobiology*, 20, 572
- Harris, C. R., Millman, K. J., van der Walt, S. J., et al. 2020, *Nature*, 585, 357–362
- Harrison, J. 2015, *Atmospheric Measurement Techniques*, 8, 3197
- . 2018, *Atmospheric Measurement Techniques*, 11, 5827
- Hermans, C., Vandaele, A. C., Carleer, M., et al. 1999, *Environmental Science and Pollution Research*, 6, 151
- Hirono, M., & Nakazawa, T. 1982, *Journal of the Physical Society of Japan*, 51, 265
- Hoinka, K. P. 1999, *Monthly Weather Review*, 127, 2248
- Hood, C. E., Fortney, J. J., Line, M. R., et al. 2020, *AJ*, 160, 198
- Howe, A. R., Burrows, A., & Deming, D. 2017, *ApJ*, 835, 96
- Hughes, R., Bernath, P., & Boone, C. 2014, *JQSRT*, 148, 18
- Humlíček, J. 1982, *Journal of Quantitative Spectroscopy and Radiative Transfer*, 27, 437
- Hunter, J. D. 2007, *Computing In Science & Engineering*, 9, 90
- Irwin, P. G. J., Teanby, N. A., de Kok, R., et al. 2008, *Journal of Quantitative Spectroscopy and Radiative Transfer*, 109, 1136
- Jiang, J. H., Zhai, A. J., Herman, J., et al. 2018, *AJ*, 156, 26
- Johns, M., McCarthy, P., Raybould, K., et al. 2012, in *Society of Photo-Optical Instrumentation Engineers (SPIE) Conference Series*, Vol. 8444, Ground-based and Airborne Telescopes IV, ed. L. M. Stepp, R. Gilmozzi, & H. J. Hall, 84441H
- Kaltenegger, L., & Lin, Z. 2021, *ApJL*, 909, L2
- Kaltenegger, L., MacDonald, R. J., Kozakis, T., et al. 2020, *ApJL*, 901, L1
- Karman, T., Gordon, I. E., van der Avoird, A., et al. 2019, *Icarus*, 328, 160
- Kasting, J. F., Pollack, J. B., & Crisp, D. 1984, *Journal of Atmospheric Chemistry*, 1, 403
- Kawahara, H. 2020, *ApJ*, 894, 58
- Kawahara, H., & Masuda, K. 2020, *ApJ*, 900, 48
- Kawauchi, K., Narita, N., Sato, B., et al. 2018, *PASJ*, 70, 84
- Keller-Rudek, H., Moortgat, G. K., Sander, R., & Sörensen, R. 2013, *Earth System Science Data*, 5, 365
- Kellmann, S., von Clarmann, T., Stiller, G. P., et al. 2012, *Atmospheric Chemistry & Physics*, 12, 11857
- Kempton, E. M.-R., Lupu, R., Owusu-Asare, A., Slough, P., & Cale, B. 2017, *Publications of the Astronomical Society of the Pacific*, 129, 044402
- Kendrew, S., Scheithauer, S., Bouchet, P., et al. 2015, *PASP*, 127, 623
- Kitzmann, D., Heng, K., Oreshenko, M., et al. 2019, *arXiv:1910.01070*
- Knutson, H. A., Benneke, B., Deming, D., & Homeier, D. 2014, *Nature*, 505, 66
- Kochanov, R. V., Gordon, I. E., Rothman, L. S., et al. 2019, *JQSRT*, 230, 172
- Komacek, T. D., Fauchez, T. J., Wolf, E. T., & Abbot, D. S. 2020, *ApJL*, 888, L20
- Kopparapu, R., Arney, G., Haqq-Misra, J., Lustig-Yaeger, J., & Villanueva, G. 2021, *ApJ*, 908, 164
- Kreidberg, L., Bean, J. L., Désert, J.-M., et al. 2014, *Nature*, 505, 69
- Kreidberg, L., Line, M. R., Bean, J. L., et al. 2015, *The Astrophysical Journal*, 814, 66

- Krissansen-Totton, J., & Fortney, J. J. 2022, *ApJ*, 933, 115
- Krissansen-Totton, J., Garland, R., Irwin, P., & Catling, D. C. 2018, *AJ*, 156, 114
- Lacy, B. I., & Burrows, A. 2020, *ApJ*, 905, 131
- Lafferty, W. J., Solodov, A. M., Weber, A., Olson, W. B., & Hartmann, J.-M. 1996, *ApOpt*, 35, 5911
- Lamsal, L. N., Martin, R. V., Parrish, D. D., & Krotkov, N. A. 2013, *Environmental Science and Technology*, 47, 7855
- Lavie, B., Mendonça, J. M., Mordasini, C., et al. 2016, *ArXiv e-prints*, arXiv:1610.03216
- Lavie, B., Mendonça, J. M., Mordasini, C., et al. 2017, *AJ*, 154, 91
- Lee, Y. J., Sagawa, H., Haus, R., et al. 2016, *Journal of Geophysical Research (Planets)*, 121, 1737
- Léger, A., Fontecave, M., Labeyrie, A., et al. 2011, *Astrobiology*, 11, 335
- Léger, A., Pirre, M., & Marceau, F. J. 1993, *A&A*, 277, 309
- Leung, M., Meadows, V. S., & Lustig-Yaeger, J. 2020, *AJ*, 160, 11
- Lin, H. W., Gonzalez Abad, G., & Loeb, A. 2014, *ApJL*, 792, L7
- Lin, Z., MacDonald, R. J., Kaltenegger, L., & Wilson, D. J. 2021, *MNRAS*, 505, 3562
- Lincowski, A. P., Lustig-Yaeger, J., & Meadows, V. S. 2019, *The Astronomical Journal*, 158, 26
- Lincowski, A. P., Meadows, V. S., Crisp, D., et al. 2018, *ApJ*, 867, 76
- . 2021, *ApJL*, 908, L44
- Line, M. R., Knutson, H., Wolf, A. S., & Yung, Y. L. 2014, *The Astrophysical Journal*, 783, 70
- Line, M. R., & Parmentier, V. 2016, *ApJ*, 820, 78
- Line, M. R., Wolf, A. S., Zhang, X., et al. 2013, *The Astrophysical Journal*, 775, 137
- Livengood, T. A., Deming, L. D., A’Hearn, M. F., et al. 2011, *Astrobiology*, 11, 907
- Loftus, K., Wordsworth, R. D., & Morley, C. V. 2019, *arXiv e-prints*, arXiv:1908.02769
- Luger, R., Sestovic, M., Kruse, E., et al. 2017, *Nature Astronomy*, 1, 0129
- Lustig-Yaeger, J., Meadows, V. S., & Lincowski, A. P. 2019, *AJ*, 158, 27
- Lustig-Yaeger, J., Meadows, V. S., Tovar Mendoza, G., et al. 2018, *AJ*, 156, 301
- Lustig-Yaeger, J., Sotzen, K. S., Stevenson, K. B., et al. 2022, *AJ*, 163, 140
- Lustig-Yaeger, J., Fu, G., May, E. M., et al. 2023, *arXiv e-prints*, arXiv:2301.04191
- Macdonald, E., & Cowan, N. 2023, *Earth’s transit spectrum from Macdonald and Cowan (2019)*, doi:10.5281/zenodo.8280710
- Macdonald, E. J. R., & Cowan, N. B. 2019, *MNRAS*, 489, 196
- MacDonald, R. J., & Batalha, N. E. 2023, *Research Notes of the American Astronomical Society*, 7, 54
- MacDonald, R. J., Goyal, J. M., & Lewis, N. K. 2020, *arXiv e-prints*, arXiv:2003.11548
- MacDonald, R. J., & Madhusudhan, N. 2017, *MNRAS*, 469, 1979
- Madhusudhan, N., & Seager, S. 2009, *The Astrophysical Journal*, 707, 24
- Marconi, A., Di Marcantonio, P., D’Odorico, V., et al. 2016, in *Society of Photo-Optical Instrumentation Engineers (SPIE) Conference Series*, Vol. 9908, *Ground-based and Airborne Instrumentation for Astronomy VI*, ed. C. J. Evans, L. Simard, & H. Takami, 990823
- Marinova, M. M., McKay, C. P., & Hashimoto, H. 2005, *Journal of Geophysical Research (Planets)*, 110, E03002
- Maté, B., Lugez, C., Fraser, G. T., & Lafferty, W. J. 1999, *J. Geophys. Res.*, 104, 30,585
- May, E. M., Taylor, J., Komacek, T. D., Line, M. R., & Parmentier, V. 2021, *ApJL*, 911, L30
- Mayorga, L., Lustig-Yaeger, J., May, E., et al. 2021, *The Planetary Science Journal*, 2, 140
- Mayorga, L. C., Charbonneau, D., & Thorngren, D. P. 2020, *arXiv e-prints*, arXiv:2009.05467
- Mayorga, L. C., Jackiewicz, J., Rages, K., et al. 2016, *AJ*, 152, 209
- Meadows, V. S., & Barnes, R. K. 2018, *Factors Affecting Exoplanet Habitability*, 57
- Meadows, V. S., & Crisp, D. 1996, *J. Geophys. Res.*, 101, 4595
- Meadows, V. S., & Graham, H. 2022, in *2022 Astrobiology Science Conference*, AGU
- Meadows, V. S., Lincowski, A. P., & Lustig-Yaeger, J. 2023, *The Feasibility of Detecting Biosignatures in the TRAPPIST-1 Planetary System with JWST*
- Meadows, V. S., Reinhard, C. T., Arney, G. N., et al. 2018a, *Astrobiology*, 18, 630
- Meadows, V. S., Arney, G. N., Schwieterman, E. W., et al. 2018b, *Astrobiology*, 18, 133
- Mikal-Evans, T. 2022, *MNRAS*, 510, 980
- Misra, A., Meadows, V., & Crisp, D. 2014, *The Astrophysical Journal*, 792, 61
- Moore, J. F. 1972, *PhD thesis*, COLUMBIA UNIVERSITY.
- Moran, S. E., Stevenson, K. B., Sing, D. K., et al. 2023, *ApJL*, 948, L11

- Moreau, G., Boissoles, J., Le Doucen, R., et al. 2001, *Journal of Quantitative Spectroscopy and Radiative Transfer*, 69, 245
- Morley, C. V., Kreidberg, L., Rustamkulov, Z., Robinson, T., & Fortney, J. J. 2017, *ApJ*, 850, 121
- National Academies of Sciences, Engineering, and Medicine. 2018, *Exoplanet Science Strategy* (Washington, D.C.: National Academies Press), doi:10.17226/25187
- Pallé, E., Zapatero Osorio, M. R., Barrena, R., Montañés-Rodríguez, P., & Martín, E. L. 2009, *Nature*, 459, 814
- Pandas Development Team, T. 2020, *pandas-dev/pandas: Pandas*, doi:10.5281/zenodo.3509134
- Perrin, M., & Hartmann, J. 1989, *Journal of Quantitative Spectroscopy and Radiative Transfer*, 42, 311
- Pidhorodetska, D., Fauchez, T., Villanueva, G., Domagal-Goldman, S., & Kopparapu, R. K. 2020, *arXiv e-prints*, arXiv:2001.01338
- Pluriel, W., Zingales, T., Leconte, J., & Parmentier, V. 2020, *A&A*, 636, A66
- Pollack, J. B., Dalton, J. B., Grinspoon, D., et al. 1993, *Icarus*, 103, 1
- Pontoppidan, K. M., Pickering, T. E., Laidler, V. G., et al. 2016, in *Proc. SPIE, Vol. 9910, Observatory Operations: Strategies, Processes, and Systems VI*, 991016
- Price-Whelan, A. M., Sipőcz, B. M., Günther, H. M., et al. 2018, *AJ*, 156, 123
- Quanz, S. P., Absil, O., Angerhausen, D., et al. 2019, *arXiv e-prints*, arXiv:1908.01316
- Rao, K. N. 2012, *Spectroscopy of the Earth's atmosphere and interstellar medium* (Academic Press)
- Remedios, J. J., Leigh, R. J., Waterfall, A. M., et al. 2007, *Atmospheric Chemistry & Physics Discussions*, 7, 9973
- Robinson, T. D. 2017a, *ApJ*, 836, 236
- . 2017b, *ArXiv e-prints*, arXiv:1701.05205
- Robinson, T. D., & Crisp, D. 2018, *JQSRT*, 211, 78
- Robinson, T. D., Ennico, K., Meadows, V. S., et al. 2014a, *ApJ*, 787, 171
- Robinson, T. D., Maltagliati, L., Marley, M. S., & Fortney, J. J. 2014b, *Proceedings of the National Academy of Science*, 111, 9042
- Robinson, T. D., Meadows, V. S., & Crisp, D. 2010, *ApJL*, 721, L67
- Robinson, T. D., & Salvador, A. 2023, *PSJ*, 4, 10
- Robinson, T. D., Meadows, V. S., Crisp, D., et al. 2011, *Astrobiology*, 11, 393
- Rocchetto, M., Waldmann, I. P., Venot, O., Lagage, P. O., & Tinetti, G. 2016, *ApJ*, 833, 120
- Rotman, Y., Komacek, T. D., Villanueva, G. L., Fauchez, T. J., & May, E. M. 2023, *ApJL*, 942, L4
- Rugheimer, S., Kaltenegger, L., Segura, A., Linsky, J., & Mohanty, S. 2015, *ApJ*, 809, 57
- Sagan, C., Thompson, W. R., Carlson, R., Gurnett, D., & Hord, C. 1993, *Nature*, 365, 715
- Schlawin, E., Leisenring, J., McElwain, M. W., et al. 2021, *AJ*, 161, 115
- Schneider, J., Léger, A., Fridlund, M., et al. 2010, *Astrobiology*, 10, 121
- Schreier, F., Städt, S., Hedelt, P., & Godolt, M. 2018, *Molecular Astrophysics*, 11, 1
- Schwieterman, E. W., Cockell, C. S., & Meadows, V. S. 2015a, *Astrobiology*, 15, 341
- Schwieterman, E. W., Robinson, T. D., Meadows, V. S., Misra, A., & Domagal-Goldman, S. 2015b, *ApJ*, 810, 57
- Schwieterman, E. W., Kiang, N. Y., Parenteau, M. N., et al. 2018, *Astrobiology*, 18, 663
- Seager, S., & Sasselov, D. D. 2000, *ApJ*, 537, 916
- Segura, A., Kasting, J. F., Meadows, V., et al. 2005, *Astrobiology*, 5, 706
- Segura, A., Krelove, K., Kasting, J. F., et al. 2003, *Astrobiology*, 3, 689
- Skidmore, W., TMT International Science Development Teams, & Science Advisory Committee, T. 2015, *Research in Astronomy and Astrophysics*, 15, 1945
- Snellen, I. A. G., de Kok, R. J., le Poole, R., Brogi, M., & Birkby, J. 2013, *ApJ*, 764, 182
- Snellen, I. A. G., Désert, J.-M., Waters, L. B. F. M., et al. 2017, *AJ*, 154, 77
- Speagle, J. S. 2020, *MNRAS*, 493, 3132
- Stamnes, K., Tsay, S. C., Jayaweera, K., & Wiscombe, W. 1988, *ApOpt*, 27, 2502
- Stamnes, K., Tsay, S. C., Jayaweera, K., et al. 2017, *DISORT: DIScrete Ordinate Radiative Transfer*, ascl:1708.006
- Stevenson, K. B., & Fowler, J. 2019, *Analyzing Eight Years of Transiting Exoplanet Observations Using WFC3's Spatial Scan Monitor*, *Space Telescope WFC Instrument Science Report*, arXiv:1910.02073
- STScI Development Team. 2013, *pysynphot: Synthetic photometry software package*, *Astrophysics Source Code Library*, ascl:1303.023
- Suissa, G., Mandell, A. M., Wolf, E. T., et al. 2020, *ApJ*, 891, 58
- The JWST Transiting Exoplanet Community Early Release Science Team, Ahrer, E.-M., Alderson, L., et al. 2022, *arXiv e-prints*, arXiv:2208.11692
- Tremblay, L., Line, M. R., Stevenson, K., et al. 2020, *AJ*, 159, 117
- Tribbett, P. D., Robinson, T. D., & Koskinen, T. T. 2021, *PSJ*, 2, 109

- Ugolnikov, O. S., Punanova, A. F., & Krushinsky, V. V. 2013, *JQSRT*, 116, 67
- van der Walt, S., Colbert, S. C., & Varoquaux, G. 2011, *Computing in Science and Engineering*, 13, 22
- Van Grootel, V., Fernandes, C. S., Gillon, M., et al. 2018, *ApJ*, 853, 30
- Van Vleck, J. H., & Weisskopf, V. F. 1945, *Reviews of Modern Physics*, 17, 227
- Vidal-Madjar, A., Arnold, L., Ehrenreich, D., et al. 2010, *A&A*, 523, A57
- Virtanen, P., Gommers, R., Oliphant, T. E., et al. 2019, *arXiv e-prints*, arXiv:1907.10121
- Virtanen, P., Gommers, R., Oliphant, T. E., et al. 2020, *Nature Methods*, 17, 261
- Waldmann, I. P., Tinetti, G., Rocchetto, M., et al. 2015, *The Astrophysical Journal*, 802, 107
- Wardenier, J. P., Parmentier, V., & Lee, E. K. H. 2022, *MNRAS*, 510, 620
- Webb, R. K., Brogi, M., Gandhi, S., et al. 2020, *MNRAS*, 494, 108
- West, R., Crisp, D., & Chen, L. 1990, *JQSRT*, 43, 191
- Wordsworth, R., Forget, F., & Eymet, V. 2010, *Icarus*, 210, 992
- Wunderlich, F., Godolt, M., Grenfell, J. L., et al. 2019, *A&A*, 624, A49
- Wunderlich, F., Scheucher, M., Godolt, M., et al. 2020, *ApJ*, 901, 126
- Yan, F., Fosbury, R. A. E., Petr-Gotzens, M. G., et al. 2015, *International Journal of Astrobiology*, 14, 255
- Youngblood, A., Arney, G. N., García Muñoz, A., et al. 2020, *AJ*, 160, 100
- Zhang, M., Chachan, Y., Kempton, E. M. R., & Knutson, H. A. 2019, *PASP*, 131, 034501
- Zonca, A., Singer, L., Lenz, D., et al. 2019, *Journal of Open Source Software*, 4, 1298

APPENDIX

A. REFRACTION PATH LENGTH EFFECTS

Refraction is widely appreciated as a mechanism that can set the continuum of exoplanet transmission spectra, much like a cloud deck (García Muñoz et al. 2012; Bétrémieux & Kaltenegger 2014; Misra et al. 2014). However, in solar occultation geometry with an orbiting observer, this limiting exoplanet-analog refraction effect is not immediately realized, despite the unavoidable presence of refraction in the observed transmittance data. To investigate the role of refraction in our transmission spectrum retrievals, we activated the ray tracing refraction module within SMART (Robinson 2017a) for use in our retrieval forward model, and performed a series of spectroscopic and inference tests. To accurately simulate the increase in optical path length through the atmosphere due to refraction without modeling the critical refraction boundary for an exoplanet observer at infinity, we increased the stellar radius in our radiative transfer model to the arbitrarily large value $100 R_{\odot}$. Although this change would strongly scale the transit depth $(R_p/R_s)^2$, it does not modify the resultant effective transit altitude, with the exception of the increase in optical path length that is of interest.

We took the best-fitting “cold” spectral model from our high-resolution retrieval in the $6 \mu\text{m}$ window (see Table 8) and simulated the spectrum again with refraction turned on. Figure 12 compares the spectral models with and without refraction and provides an assessment of their differences as a function of wavelength and altitude. At all wavelengths, the model with refraction results in slightly larger effective transit altitudes. Shortward of $5.5 \mu\text{m}$, where the continuum altitude within the spectral window is the lowest, the difference between the two models is largest. This distinction is most evident in the right panel of Figure 12, which shows that the model differences due to refraction are systematically larger at the lowest altitudes probed by the transmission spectrum, while the cores of the strongest lines that extend up to high altitudes are essentially unaffected by refraction. The zoomed inset provides a visual aid for this effect as the differences due to refraction increase stepping down from the strongest H_2O and CO_2 lines—where there is no discernible refraction effects—to the weakest lines and the continuum—where the refraction effects are

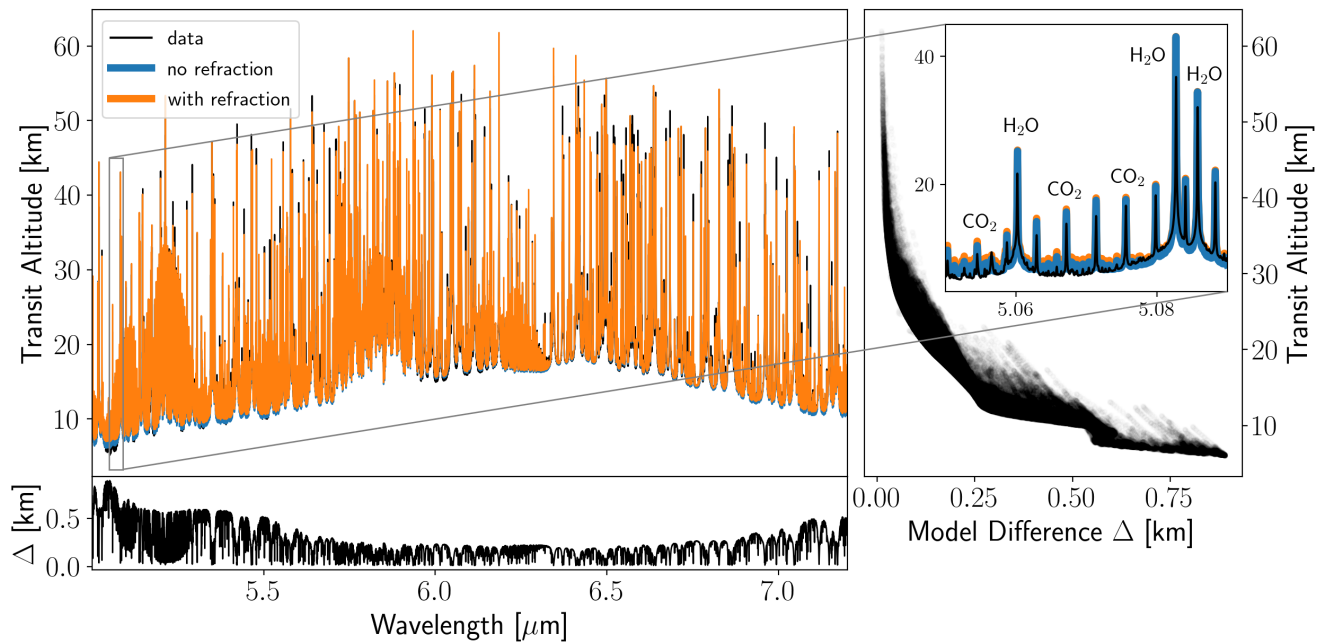


Figure 12. Comparison of transmission spectrum models with and without refraction. The upper left panel shows the two spectral models atop the observed data in the $6 \mu\text{m}$ band of interest. The lower left panel shows the residuals between the model with and without refraction, which appears anti-correlated with the spectral continuum. This relationship is borne out more clearly in the right panel, which shows the model residuals as a function of transit altitude where larger model difference due to refraction are observed at lower altitudes. Finally, the zoomed inset visually emphasizes this point by showing a comparison of individual CO_2 and H_2O lines. The cores of optically thick lines that probe higher altitudes are not affected by refraction, while the continuum, and optically thin line and cores are slightly affected, with larger refraction effects seen at lower altitudes.

maximal. Although this demonstrates the existence of a systematic modeling artifact due to the omission of refraction physics, and the resultant increase in optical path length, the maximum model deviations seen near the continuum still remain quite small (< 1 km) and are exceeded by the average deviations of our best fitting models.

B. SIMULATED JWST RETRIEVAL POSTERIOR & TESTS

Figure 13 shows a corner plot of the posterior distributions retrieved for TRAPPIST-1e from simulated NIRSpec G395M and MIRI LRS observations, as discussed in Section 3.3 and Figure 11.

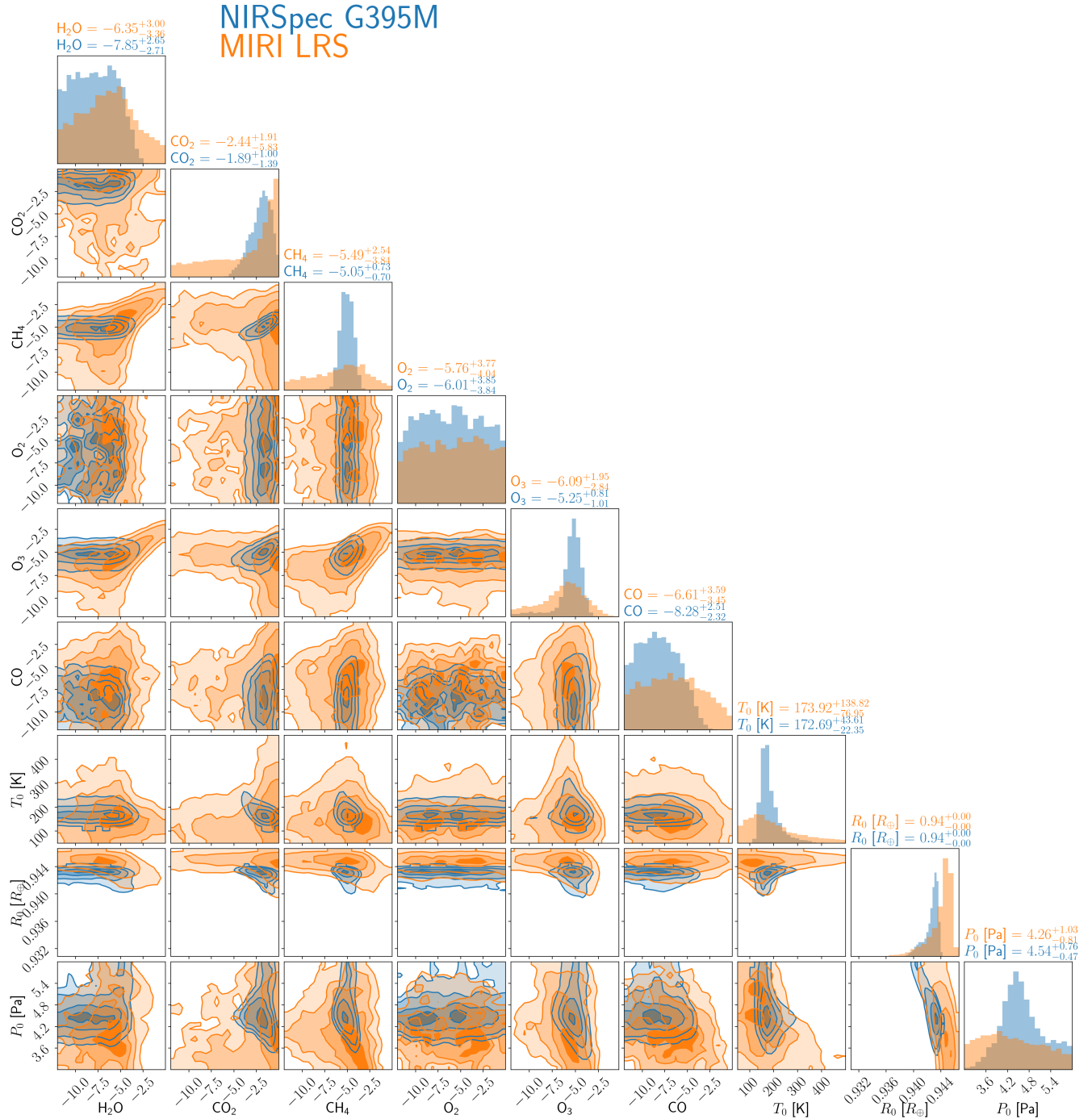


Figure 13. Marginalized posterior distributions for the NIRSpec G395M (blue) and MIRI LRS (orange) retrievals discussed in Section 3.3 and Figure 11. These constraints correspond to 80 stacked transits of TRAPPIST-1e using each instrument.

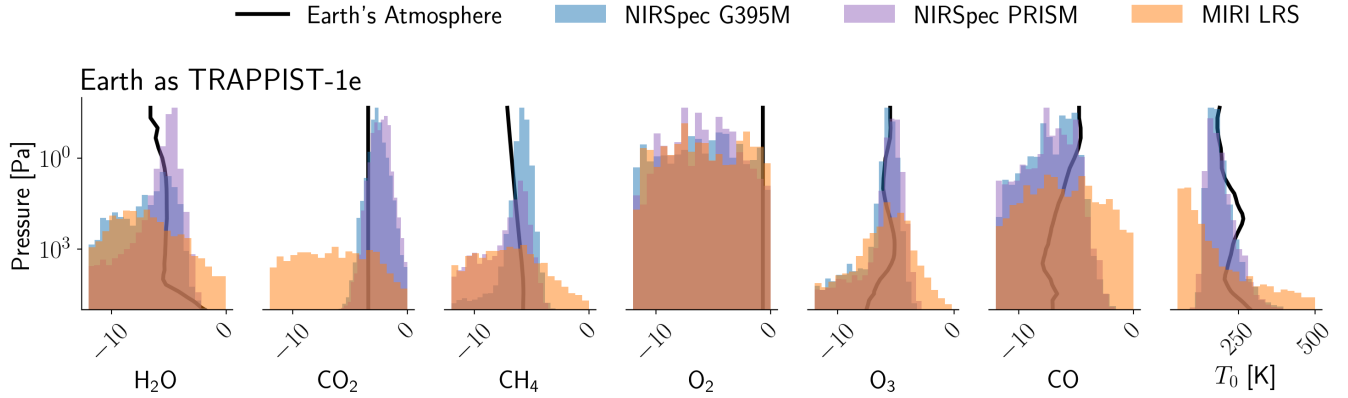


Figure 14. 1-D marginalized posterior distributions for NIRSpec G395M (blue), NIRSpec PRISM (purple), and MIRI LRS (orange) retrievals. These constraints correspond to 80 stacked transits of TRAPPIST-1e using each instrument, but in this case without randomized noise added to the observations.

We also investigated a limited case using the NIRSpec PRISM instrument mode. Figure 14 is similar to the upper panel of Figure 11 with the addition of retrieval results from a simulated spectrum using the NIRSpec PRISM mode with a shortwave cutoff of $2.2 \mu\text{m}$. All results are shown for retrievals where the data points were centered on their true model value (similar to, for example, Feng et al. (2018), but unlike our Figure 11) to also investigate the sensitivity of our results to the specific random noise instance that was previously used. The G395M and PRISM results are very similar, likely due to the fact that we could not include Earth data for the PRISM case shortward of $2.2 \mu\text{m}$ so the two modes cover a similar wavelength range, but differ in spectral resolution (PRISM has $R \sim 100$ and G395M has $R \sim 1000$). However, given this caveat, the PRISM data yields slightly higher sensitivity to H_2O and the G395M data yields slightly higher sensitivity to CH_4 . The high abundance CO_2 posterior spike seen for MIRI LRS in Figure 11 is absent in this test, thereby demonstrating that it was a manifestation of random noise.